Monthly Notices
of the
ROYAL ASTRONOMICAL SOCIETY

MNRAS **494,** 6012–6029 (2020)
Advance Access publication 2020 April 26

doi:10.1093/mnras/staa1129

The unusual broad-band X-ray spectral variability of NGC 1313 X-1 seen with *XMM–Newton*, *Chandra*, and *NuSTAR*

D. J. Walton [1★] C. Pinto,[2,3] M. Nowak,[4] M. Bachetti [5] R. Sathyaprakash,[6] E. Kara [7] T. P. Roberts,[6] R. Soria,[8,9] M. Brightman,[10] C. R. Canizares,[7] H. P. Earnshaw [10] F. Fürst,[11] M. Heida [12] M. J. Middleton,[13] D. Stern,[14] L. Tao [15] N. Webb,[16] W. N. Alston [1] D. Barret,[16] A. C. Fabian [1] F. A. Harrison[10] and P. Kosec[1]

Affiliations are listed at the end of the paper

Accepted 2020 April 20. Received 2020 April 20; in original form 2019 November 20

ABSTRACT

We present results from the major coordinated X-ray observing programme on the ULX NGC 1313 X-1 performed in 2017, combining *XMM–Newton*, *Chandra*, and *NuSTAR*, focusing on the evolution of the broad-band (∼0.3–30.0 keV) continuum emission. Clear and unusual spectral variability is observed, but this is markedly suppressed above ∼10–15 keV, qualitatively similar to the ULX Holmberg IX X-1. We model the multi-epoch data with two-component accretion disc models designed to approximate super-Eddington accretion, allowing for both a black hole and a neutron star accretor. With regards to the hotter disc component, the data trace out two distinct tracks in the luminosity–temperature plane, with larger emitting radii and lower temperatures seen at higher observed fluxes. Despite this apparent anticorrelation, each of these tracks individually shows a positive luminosity–temperature relation. Both are broadly consistent with $L \propto T^4$, as expected for blackbody emission with a constant area, and also with $L \propto T^2$, as may be expected for an advection-dominated disc around a black hole. We consider a variety of possibilities for this unusual behaviour. Scenarios in which the innermost flow is suddenly blocked from view by outer regions of the super-Eddington disc/wind can explain the luminosity–temperature behaviour, but are difficult to reconcile with the lack of strong variability at higher energies, assuming this emission arises from the most compact regions. Instead, we may be seeing evidence for further radial stratification of the accretion flow than is included in the simple models considered, with a combination of winds and advection resulting in the suppressed high-energy variability.

Key words: X-rays: binaries – X-rays: individual: NGC 1313 X-1.

1 INTRODUCTION

NGC 1313 X-1 is one of the archetypal ultraluminous X-ray sources (ULXs). These are off-nuclear X-ray sources that appear to radiate in excess of 10^{39} erg s^{-1}, roughly the Eddington limit for the stellar remnant black holes ($M_{\rm BH} \sim 10\,{\rm M}_{\odot}$) that power X-ray binaries in our own Galaxy (see Kaaret, Feng & Roberts 2017 for a recent review). Although they were historically considered good candidates for hosting intermediate-mass black holes (IMBHs, $M_{\rm BH} \sim 10^{2–5}\,{\rm M}_{\odot}$; e.g. Miller et al. 2003, 2004; Miller & Colbert 2004; Strohmayer & Mushotzky 2009), the broad-band X-ray spectra observed in the *NuSTAR* era show clear deviations from the standard sub-Eddington accretion modes which would be expected for such objects (e.g. Bachetti et al. 2013; Walton et al. 2013, 2014, 2015a,b, 2017; Sazonov, Lutovinov & Krivonos 2014; Annuar et al. 2015; Mukherjee et al. 2015; Rana et al. 2015; Luangtip, Roberts & Done 2016; Krivonos & Sazonov 2016; Fürst et al. 2017; Shidatsu, Ueda & Fabrika 2017). These observations confirmed the previous indications for these deviations seen in the more limited *XMM–Newton* bandpass (Stobbart, Roberts & Wilms 2006; Gladstone, Roberts & Done 2009), and imply instead that the majority of ULXs likely represent a population of X-ray binaries accreting at high/super-Eddington rates.

This conclusion was further cemented with the remarkable discovery that a number of ULXs are actually powered by accreting pulsars (Bachetti et al. 2014; Fürst et al. 2016; Israel et al. 2017a,b; Carpano et al. 2018; Rodríguez Castillo et al. 2019; Sathyaprakash et al. 2019). These sources therefore appear to exceed their Eddington limits by factors of up to ∼500, and their broad-band spectra are

★ E-mail: dwalton@ast.cam.ac.uk

qualitatively similar to the rest of the ULX population, particularly at high energies ($E > 10$ keV; Koliopanos et al. 2017; Pintore et al. 2017; Walton et al. 2018b,c). Two other ULXs in M51 have also been identified as likely hosting neutron star accretors via other means, first through the detection of a potential cyclotron resonant scattering feature (Brightman et al. 2018), and second through the detection of a potentially bi-modal flux distribution (as expected for a source transitioning to and from the propeller regime; Earnshaw, Roberts & Sathyaprakash 2018). A number of other candidates for such transitions have also recently been reported among the broader ULX population (Song et al. 2020). Although the known ULX pulsars are now firmly established as being powered by magnetized neutron stars, the strength of the magnetic fields in these systems is still the subject of significant debate, with estimates ranging from $\sim 10^{9-15}$ G and some models invoking higher order field geometries (e.g. quadrupolar) than the standard dipole fields typically assumed (e.g. Bachetti et al. 2014; Dall'Osso, Perna & Stella 2015; Kluźniak & Lasota 2015; Mushtukov et al. 2015; Fürst et al. 2016; Brightman et al. 2018; Vasilopoulos et al. 2018; Walton et al. 2018a; Middleton et al. 2019).

One of the fundamental predictions of super-Eddington accretion is that strong winds are launched from the accretion flow, as radiation pressure exceeds gravity (e.g. Shakura & Sunyaev 1973; Poutanen et al. 2007; Dotan & Shaviv 2011; Takeuchi, Ohsuga & Mineshige 2013). Observational evidence for such winds in ULXs was only recently seen for the first time in NGC 1313 X-1, through the detection of strongly blueshifted atomic features (Pinto, Middleton & Fabian 2016; Walton et al. 2016a; see also Middleton et al. 2015b), and such features have now been seen in several other systems (including NGC 300 ULX1, one of the known pulsars; Pinto et al. 2017; Kosec et al. 2018a,b). These winds are extreme, reaching velocities of up to $\sim 0.25c$, and, despite the extreme X-ray luminosities of these sources, may actually dominate their total energetic output.

In order to study the variability of the extreme outflow in NGC 1313 X-1, we performed a series of coordinated broad-band X-ray observations of the NGC 1313 galaxy combining data from *XMM–Newton* (PI: Pinto), *Chandra* (PI: Canizares), and *NuSTAR* (PI: Walton). This programme has already provided a variety of interesting results, revealing clear variability in the wind in X-1 (Pinto et al. 2020), a ~ 150 s soft X-ray lag in X-1 (Kara et al. 2020), and the detection of pulsations in X-2 (Sathyaprakash et al. 2019). Here we combine these observations with the coordinated *XMM–Newton* and *NuSTAR* observations available in the archive to study the broad-band continuum variability exhibited by NGC 1313 X-1.

2 OBSERVATIONS AND DATA REDUCTION

During the main 2017 campaign, *XMM–Newton* (Jansen et al. 2001) observed NGC 1313 with its full suite of instrumentation for six full orbits (~ 750 ks total exposure), grouped into three pairs of observations, with the two observations constituting each pair taken in relatively quick succession. *Chandra* (Weisskopf et al. 2002) also performed a series of observations across 2017, totalling ~ 500 ks exposure. Although these *Chandra* observations are relatively well spread across the year, there are two periods where a number of the observations are clustered in time. In addition to these soft X-ray observations, *NuSTAR* (Harrison et al. 2013) also performed a series of five exposures over the second half of 2017 (~ 500 ks total exposure). One was performed with each of the pairs of *XMM–Newton* observations, taken simultaneously with one of the two exposures, and the remaining two were taken with the two main clusters of *Chandra* observations, again performed simultaneously with one of the exposures in these two groups.

Table 1. Details of the X-ray observations of NGC 1313 used in this work.

Epoch	Mission(s)	OBSID(s)	Start date	Exposure[a] (ks)
XN1	*NuSTAR*	30002035002	2012-12-16	154
	NuSTAR	30002035004	2012-12-21	206
	XMM–Newton	0693850501	2012-12-16	85/112
	XMM–Newton	0693851201	2012-12-22	79/120
XN2	*NuSTAR*	80001032002	2014-07-05	73
	XMM–Newton	0742590301	2014-07-05	54/61
XN3	*NuSTAR*	90201050002	2017-03-29	125
	XMM–Newton	0794580601	2017-03-29	25/38
XN4	*NuSTAR*	30302016002	2017-06-14	100
	XMM–Newton	0803990101	2017-06-14	110/130
	XMM–Newton	0803990201	2017-06-20	111/129
CN1	*NuSTAR*	30302016004	2017-07-17	87
	Chandra	19929	2017-07-03	18
	Chandra	20105	2017-07-06	31
	Chandra	19712	2017-07-18	49
	Chandra	20125	2017-08-01	25
	Chandra	20126	2017-08-02	27
	Chandra	19714	2017-08-03	20
	Chandra	19927	2017-08-05	25
XN5	*NuSTAR*	30302016006	2017-09-03	90
	XMM–Newton	0803990301	2017-08-31	45/101
	XMM–Newton	0803990401	2017-09-02	83/81
CN2	*NuSTAR*	30302016008	2017-09-15	108
	Chandra	19928	2017-08-28	21
	Chandra	20729	2017-09-16	10
	Chandra	20637	2017-09-24	28
	Chandra	19713	2017-09-26	32
	Chandra	20798	2017-09-29	17
XN6[b]	*NuSTAR*	30302016010	2017-12-09	100
	XMM–Newton	0803990601	2017-12-09	69/115

Notes. [a]Good exposures used for our spectral analysis, given to the nearest ks; *XMM–Newton* exposures are listed for the EPIC-pn/MOS detectors, and the *NuSTAR* exposures combine both modes 1 and 6 (see Section 2.1).
[b]Although two *XMM–Newton* observations were taken as part of epoch XN6, the two show markedly different spectra, so we only make use of the *XMM–Newton* observation taken simultaneously with the *NuSTAR* exposure for this epoch (see Section 3.1).

In addition to these observations, *XMM–Newton* and *NuSTAR* have also performed coordinated observations on a few prior occasions. There were two deep observations taken in quick succession soon after the launch of *NuSTAR* in 2012 (see Bachetti et al. 2013; Miller et al. 2014; Walton et al. 2016a), as well as shorter coordinated observations taken in 2014 and again in 2017 prior to the commencement of the main campaign. Details of the observations considered in this work are given in Table 1, and the following sections describe our data reduction procedure for the various missions involved.

2.1 *NuSTAR*

We reduced the *NuSTAR* data as standard with the *NuSTAR* Data Analysis Software (v1.8.0; part of the HEASOFT distribution) and *NuSTAR* CALDB v20171204. The unfiltered event files were cleaned with NUPIPELINE. We used the standard depth correction, which

significantly reduces the internal background at high energies, and periods of earth-occultation and passages through the South Atlantic Anomaly were also excluded. To be conservative, source products were extracted from circular regions of radius 30 arcsec, owing to the presence of another faint source to the south (see Bachetti et al. 2013), and the background was estimated from a larger, blank area on the same detector, free of contaminating point sources (the exact size of the background region used varies between epochs, depending on the position angle of the observation and the proximity of the source to the edge of the detector). Spectra and light curves were extracted from the cleaned event files using NUPRODUCTS for both focal plane modules (FPMA and FPMB). In addition to the standard 'science' data (mode 1), we also extract the 'spacecraft science' data (mode 6) following Walton et al. (2016b). This provides ∼20–40 per cent of the total good exposure, depending on the specific observation.

2.2 *XMM–Newton*

For the *XMM–Newton* observations, data reduction was carried out with the *XMM–Newton* Science Analysis System (SAS v16.1.0). Here we focus on the data taken by the EPIC CCD detectors – EPIC-pn and EPIC-MOS (Strüder et al. 2001; Turner et al. 2001) – for our continuum analysis; the high-resolution data from the Reflection Grating Spectrometer (RGS; den Herder et al. 2001) is presented in a separate work (Pinto et al. 2020). The raw observation data files were processed as standard using EPCHAIN and EMCHAIN. Source products were extracted from circular regions of radius ∼30 arcsec, and, as before, the background was estimated from larger areas on the same CCD free from contaminating point sources (again, the exact size of the background region used varies from epoch to epoch, depending on the position angle of the observation and, for the EPIC-pn detector, the position of the read-out streak relative to other nearby sources). Light curves and spectra were generated with XMMSELECT, excluding periods of high background and selecting only single and double events for EPIC-pn (PATTERN ≤ 4), and single to quadruple events for EPIC-MOS (PATTERN ≤ 12). The redistribution matrices and auxiliary response files for each detector were generated with RMFGEN and ARFGEN, respectively. After performing the data reduction separately for each of the MOS detectors, and confirming their consistency, these spectra were combined using the FTOOL ADDASCASPEC for each OBSID. Finally, where spectra from different OBSIDs were merged, these were also combined using ADDASCASPEC.

2.3 *Chandra*

High spectral resolution X-ray spectroscopy is provided by the *Chandra* High Energy Gratings Spectrometer (HETGS; Canizares et al. 2005), which consists of two gratings sets: the Medium Energy Gratings (MEG, $E/\Delta E \approx 700$ at 1 keV) and the High Energy Gratings (HEG, $E/\Delta E \approx 1300$ at 1 keV). Each gratings set, MEG and HEG, disperses spectra into negative and positive orders. Throughout this work, as we describe below, we combine the ±1st order spectra into a single spectrum for each gratings instrument (appreciable counts in the higher orders are only obtained for very bright sources, so are ignored in our analyses). The HETG also produces an undispersed 0th order spectrum, but it suffers from photon pile-up (Davis 2001), so we do not consider it further.

The *Chandra*-HETG spectra were created using the Interactive Spectral Interpretation System (ISIS; Houck & Denicola 2000) running extraction scripts from the Transmission Gratings Catalogue (TGcat; Huenemoerder et al. 2011). These scripts in turn ran tools from CIAO v4.10 and utilized *Chandra* CALDB v4.7.8. The position of the 0th order image was determined by the TGDETECT tool, which then defined the identification and extraction regions for the ±1st orders of the MEG and HEG. Specifically, events within an 18 pixel radius of the 0th order image were assigned to 0th order, while any events that fell within ±18 pixels of the cross dispersion direction of either the MEG or HEG spectra were assigned to that grating arm using the TG_CREATE_MASK tool. In overlap regions, events are preferentially assigned to 0th, MEG, and then HEG, respectively. Within these identification regions, events that were within ±1 arcsec of the HEG and MEG dispersion arm locations were extracted (TG_EXTRACT) and assigned to a given spectral order with TG_RESOLVE_EVENTS using the default settings, while background spectra were extracted from regions that lay 3–8.5 arcsec perpendicularly from the dispersion arm locations. The standard tools, FULLGARF and MKGRMF, were used to create the spectral response matrices. Finally, for a given set of gratings (HEG or MEG) the spectra were combined for ±1st orders using ADDASCASPEC for each OBSID, and where spectra from multiple OBSIDs were combined we again used ADDASCASPEC.

3 SPECTRAL ANALYSIS

Our focus on this work is on broad-band spectroscopy of NGC 1313 X-1. All of the data sets analysed are rebinned to have a signal-to-noise (S/N) ratio of at least 5 per energy bin, using a combination of SPECGROUP in the *XMM–Newton* SAS and custom software, and we fit the data using χ^2 minimization. The *XMM–Newton* EPIC data sets are analysed over the 0.3–10.0 keV range, the *Chandra* MEG and HEG data over the 0.6–6.0 and 0.8–8.0 keV ranges, respectively, and the *NuSTAR* FPMA/B data provide coverage up to ∼25–35 keV, depending on the data set (above which the S/N drops below 5). We perform spectral analysis with XSPEC v12.10.0 (Arnaud 1996) throughout, and quote parameter uncertainties at the 90 per cent confidence level for one interesting parameter ($\Delta\chi^2 = 2.7$). We allow multiplicative constants to float between the data sets from a given epoch to account for cross-calibration uncertainties between the different detectors, with FPMA fixed at unity as one of the detectors common to all epochs; these constants are within ∼10 per cent of unity, as expected (Madsen et al. 2015). Throughout this work, we assume a distance of $D = 4.2$ Mpc to NGC 1313 (Méndez et al. 2002; Tully, Courtois & Sorce 2016).

3.1 Data organization

The observations considered are naturally grouped into several broad epochs, largely determined by the *NuSTAR* coverage; we refer to the coordinated *XMM–Newton* + *NuSTAR* epochs as XN*i*, and the coordinated *Chandra* + *NuSTAR* epochs as CN*i*, where *i* indicates the chronology for each combination (see Table 1; note that we do not require strict simultaneity between the data from the relevant observatories when defining these epochs, and that the observations combined to form each epoch are all taken within ∼2 weeks of the *NuSTAR* exposures around which they are defined). Fig. 1 shows the *NuSTAR* coverage in the context of the long-term behaviour from NGC 1313 X-1 seen by the *Neil Gehrels Swift Observatory* (hereafter *Swift*; Gehrels et al. 2004), extracted using the standard online pipeline (Evans et al. 2009). These epochs cover a range of fluxes, and also the period of enhanced variability seen more recently by *Swift* (commencing MJD ∼ 57400).

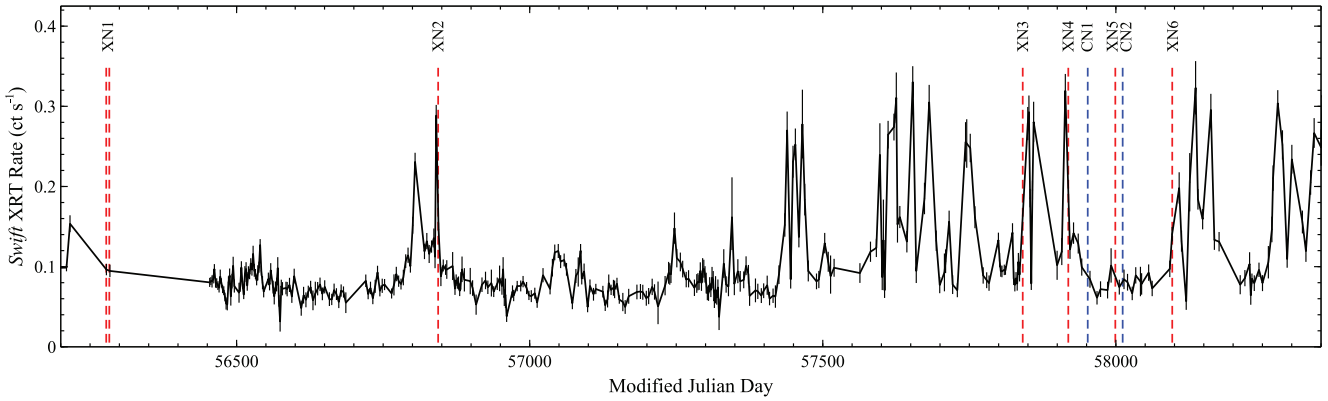

Figure 1. The long-term 0.3–10 keV X-ray light curve seen by *Swift* XRT since October 2012. The timing of the *NuSTAR* observations, which define the broad epochs considered here, is indicated by the red dashed lines for coordination with *XMM–Newton*, and blue dashed lines for coordination with *Chandra*. The period after MJD ∼ 57400 shows enhanced variability, which is covered by a number of our broad-band observations.

The two broad-band observations performed in quick succession in 2012 are considered to be a single epoch (XN1) in this work, as they both exhibit the same spectrum and there is negligible variability within either of the observations (Bachetti et al. 2013). Epoch XN4 coincidentally caught the end of a relatively large flare (see Fig. 1), with NGC 1313 X-1 showing strong flux and spectral evolution across the simultaneous *XMM–Newton* + *NuSTAR* exposure (see Fig. 2). We therefore split the data from this epoch into higher and lower flux periods, which we refer to as epochs XN4a and XN4b, respectively. The XN4a spectrum is extracted from the first 45 ks of the simultaneous exposure (OBSIDs 0803990101 and 30302016002; this is the point at which the high-energy ($E > 3$ keV) flux/spectral variability stabilizes), while the XN4b spectrum is extracted from the remaining data from these OBSIDs, combined with the second XMM–Newton exposure (OBSID 0803990201), which exhibited similar flux and spectral shape. None of the other new observations considered here show notable spectral variability within any of the individual exposures. The two *XMM–Newton* observations taken during epoch XN5 show consistent spectra, and so are combined. However, the two *XMM–Newton* observations taken during epoch XN6 do show clearly different spectra, and so in this case we only consider the *XMM–Newton* data from the exposure taken simultaneously with *NuSTAR*. We also note that, owing to the spread of the full *Chandra* data set, for epochs XN5 and XN6 there are also short *Chandra* observations contemporaneous with the *XMM–Newton* and *NuSTAR* data, but in these cases we only consider the higher S/N *XMM–Newton* data for the soft X-ray coverage. For epochs CN1 and CN2, we confirmed that the spectra from each of the individual *Chandra* observations grouped together were consistent, before combining them further into the final merged spectra used in our analysis.

3.2 Broad-band spectral variability

The nine broad-band spectra extracted are shown in Fig. 3. The spectral variability exhibited by NGC 1313 X-1 shows remarkable similarity to the behaviour seen from Holmberg IX X-1 (Walton et al. 2014, 2017; Luangtip et al. 2016), another well-studied ULX; the variability is strong at lower energies (below ∼10 keV), with the spectrum becoming more centrally peaked at higher fluxes, but the higher energy data (above ∼10 keV) appears to remain extremely similar for all of the spectra compiled to date. To illustrate this, we model the *NuSTAR* data above 10 keV with a simple power-law model. The photon indices are all consistent within their 90 per cent confidence limits (fitting all of the data sets together we find $\Gamma = 3.2 \pm 0.1$), and the 10–40 keV fluxes only vary by at most a factor of ∼1.5, despite the factor of >3 differences seen at ∼3 keV.

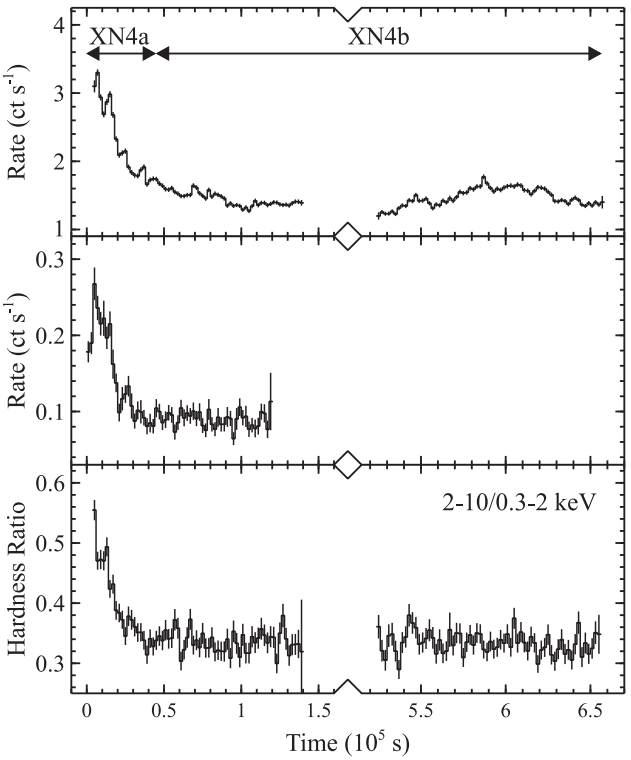

Figure 2. Light curves from the observations that form epoch XN4 (2 ks time bins). The top panel shows the 0.3–10.0 keV light curve observed with the EPIC-pn detector over the two *XMM–Newton* exposures, and the middle panel shows the 3–30 keV light curve observed with the *NuSTAR* FPMA detector. The bottom panel also shows a hardness ratio computed between the 0.3–2.0 and 2.0–10.0 keV bands, based on the EPIC-pn count rates. Clear spectral variability is seen towards the beginning of these observations, after which the spectrum appears to stabilize (even if some flux variability is still observed). For our spectral analysis, we therefore split these data into two sub-epochs, which we refer to as XN4a and XN4b, as indicated by the horizontal arrows.

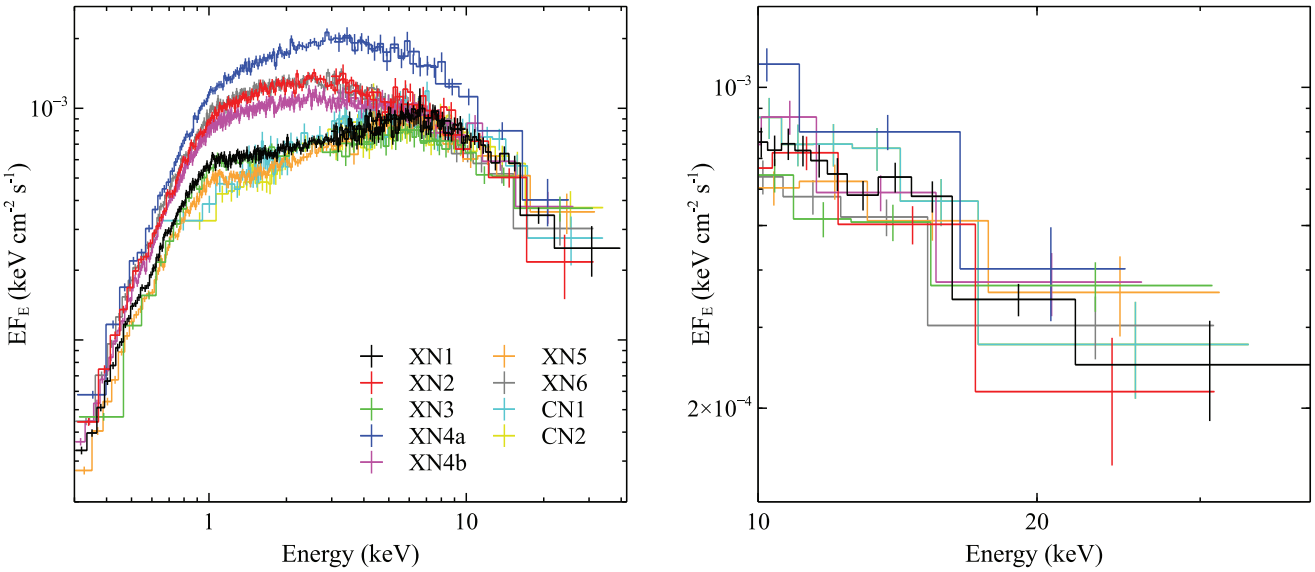

Figure 3. Left: The broad-band spectral evolution displayed by NGC 1313 X-1. For clarity, we only show the EPIC-pn data for *XMM–Newton* and the MEG data for *Chandra* (where relevant), and the FPMA data for *NuSTAR*. Given the large number of data sets shown, we show the soft and hard X-ray coverage from each epoch in the same colour. The *XMM–Newton* data span the ∼0.3–10.0 keV range, the *Chandra* data shown span the ∼0.6–6.0 keV range, and the *NuSTAR* data span the ∼3–35 keV range. Despite the strong variations at lower energies (below ∼10 keV), the higher energy data (above ∼10 keV) are relatively stable. Right: A zoom in on the high-energy (>10 keV) data from *NuSTAR* (again, FPMA only for clarity), further demonstrating the relative lack of variability observed at these energies in comparison to the lower energy data. All the data have been unfolded through a simple model that is constant with energy, and have been further rebinned for visual purposes.

As the nature of the accretor in NGC 1313 X-1 remains unknown (no pulsations have been seen from NGC 1313 X-1 to date; see Appendix A), we construct two models to fit the broad-band data that may approximate super-Eddington accretion on to a non-magnetic accretor (either a black hole or an non-magnetic neutron star; note that super-Eddington accretion on to a non-magnetic neutron star is expected to be conceptually similar to the black hole case, with a standard outer disc, a funnel-like inner region and strong winds, e.g. King 2008, although for a given luminosity the accretion rate relative to Eddington would naturally be more extreme in the former) and a magnetic accretor (i.e. a ULX pulsar), respectively, although we stress that these models are still strictly phenomenological. Throughout this work, we include two neutral absorbers in all of our modelling, the first fixed to the Galactic column of $N_{\rm H} = 4.13 \times 10^{20}$ cm^{-2} (Kalberla et al. 2005), and the second free to account for absorption local to NGC 1313 ($z = 0.001\,57$). For the neutral absorption, we use the TBABS absorption model, combining the solar abundances of Wilms, Allen & McCray (2000) and the cross-sections of Verner et al. (1996). We also note again that NGC 1313 X-1 is known to show atomic features in both absorption and emission, particularly at low energies (Middleton et al. 2014; Pinto et al. 2016; Walton et al. 2016a). However, here we are interested in the spectral variability of the continuum emission, and these features do not strongly influence the broad-band continuum fits, so we do not treat them here; instead the atomic emission/absorption will be the subject of separate works (Pinto et al. 2020; M. Nowak et al., in preparation).

3.2.1 *The non-magnetic accretor model*

For super-Eddington accretion on to a non-magnetic accretor, the structure of the accretion flow is expected to deviate from the standard thin disc approximation typically invoked for sub-Eddington accretion. As the accretion rate approaches and increases beyond the Eddington limit, the scale height of the inner regions of the disc is expected to increase, supported by the increasing radiation pressure (e.g. Shakura & Sunyaev 1973; Abramowicz et al. 1988; Poutanen et al. 2007; Dotan & Shaviv 2011). This results in a transition from a thin disc to a thicker flow roughly at the 'spherization' radius ($R_{\rm sp}$), the point at which the flow reaches the Eddington limit. Radiation pressure and potentially also advection of radiation are expected to be important for the thicker inner regions of such a flow, which modifies the radial temperature profile – typically parametrized as $T(r) \propto r^{-p}$ – of this region of the flow away from that expected for a thin disc; a standard thin disc should have $p = 0.75$ (Shakura & Sunyaev 1973), while a high-Eddington, advective flow should have $p < 0.75$ (Abramowicz et al. 1988). Strong winds are also expected to be launched from the regions interior to $R_{\rm sp}$ (e.g. Ohsuga & Mineshige 2011; Takeuchi et al. 2013), which may themselves be optically thick (and therefore contribute blackbody-like emission) and shroud the outer accretion flow (e.g. King & Pounds 2003; Urquhart & Soria 2016; Zhou et al. 2019).

We therefore use two thermal components to model the accretion flow in the scenario that the accretor is non-magnetic, combining DISKBB (Mitsuda et al. 1984) for the outer flow/optically thick wind and DISKPBB (Mineshige et al. 1994) for the inner flow. The DISKBB model assumes a thin disc profile (i.e. $p = 0.75$), while the DISKPBB model allows p to be fit as a free parameter. This combination has frequently been applied to explain the soft X-ray data ($E < 10$ keV) in spectral analyses of ULXs (e.g. Stobbart et al. 2006; Walton et al. 2014, 2017; Mukherjee et al. 2015; Rana et al. 2015)

As shown in Walton et al. (2018c), even when using complex accretion disc models such as this, all the ULXs observed by *NuSTAR* to date – including NGC 1313 X-1 – require an additional continuum component that contributes above ∼10 keV. In the case of a non-magnetic accretor, this high-energy emission would likely

be associated with Compton up-scattering of disc photons in a corona of hot electrons, as is the case in sub-Eddington black hole X-ray binaries and active galactic nuclei (e.g. Haardt & Maraschi 1991). We therefore model this emission with an additional high-energy power-law tail, using the SIMPL convolution model (Steiner et al. 2009) to avoid incorrectly extrapolating the power-law emission down to arbitrarily low energies. This component is applied to the DISKPBB component, the hotter of the two components associated with the disc, as black hole coronae are expected to be compact and centrally located (e.g. Reis & Miller 2013).

We apply this model to all of the nine broad-band data sets of NGC 1313 X-1 considered in this work simultaneously, similar to our analysis of Holmberg IX X-1 (Walton et al. 2017). Following that work, and given the similarities between the multi-epoch spectra at the highest and lowest energies, we assume a common absorption column (see also Miller et al. 2013) and a common photon index for the high energy continuum across all epochs. The global fit to the data is reasonably good, with $\chi^2 = 12\,544$ for 11 559 degrees of freedom (DoF); we give the best-fitting parameters in Table 2, and show the data/model ratios for the various data sets in Fig. 4. Although there are notable residuals at $\sim$1 keV in most cases, related to atomic emission and absorption associated with the extreme outflow which are blended in the low-resolution spectra used here (Middleton et al. 2014, 2015b; Pinto et al. 2016), the shape of the continuum emission is reasonably well reproduced. We show examples of our model fits for epochs XN3, XN4a, and XN4b (i.e. covering a range of fluxes) in Fig. 5.

3.2.2 *The magnetic accretor model*

The model we use for the case of a magnetic accretor (i.e. a ULX pulsar) is based on that discussed in Walton et al. (2018b,c). This consists of two thermal blackbody components for the accretion flow outside of the magnetosphere ($R_{\rm M}$; the point at which the magnetic field of the neutron star truncates the disc and the accreting material begins to follow the field lines instead), and an exponentially cut-off power-law component (CUTOFFPL) for the central accretion columns that form as the material flows down on to the magnetic poles. For the thermal components, we again use the DISKBB+DISKPBB combination, which has also been used in previous work on ULX pulsars; assuming that $R_{\rm M} < R_{\rm sp}$, the qualitative structure of a super-Eddington flow (thin outer disc, thick inner disc, optically thick wind) is expected to be broadly similar to the non-magnetic case for radii outside of $R_{\rm M}$. The discovery of the strong wind in the ULX pulsar NGC 300 ULX1 supports the conclusion that the super-Eddington regions of the accretion flow still form in these systems (i.e. $R_{\rm M} < R_{\rm sp}$; Kosec et al. 2018b; Mushtukov et al. 2019). For dipolar magnetic fields, this would correspond to the lower end of the predicted range of field strengths ($B \lesssim 10^{12}$). However, stronger fields could still be permitted with higher order field geometries (e.g. Israel et al. 2017a; Middleton et al. 2019).

Since pulsations have not been detected from NGC 1313 X-1 we cannot constrain the spectral shape of any accretion columns directly. We therefore take a similar approach to Walton et al. (2018c), and set its spectral parameters to the average values seen from the pulsed emission from the four ULX pulsars currently known: $\langle\Gamma\rangle = 0.59$ and $\langle E_{\rm cut}\rangle = 7.9$ keV (Brightman et al. 2016; Walton et al. 2018a,b,c). These values are similar, but are not identical to those used in Walton et al. (2018c), as NGC 300 ULX1 had not been discovered to be a ULX pulsar at that time; note that for this source we take the continuum parameters from the model that includes the cyclotron resonant scattering feature presented in Walton et al. (2018a). In the magnetized case, this component provides the bulk of the high-energy ($E > 10$ keV) emission observed by *NuSTAR* and explains the high-energy excess seen even with complex disc models; the treatment of this emission is the only difference between the non-magnetic and magnetic accretion models used here.

As with the non-magnetic case, we apply this model to all nine broad-band data sets considered in this work simultaneously, again assuming a common absorption column for all epochs (the shape of the accretion column is fixed in the model, and so is also common for all epochs). The global fit to the data is similarly good (χ^2/DoF $= 12\,572/11\,560$), with the shape of the continuum similarly well described as the non-magnetic case (we do not show the data/model ratios for the magnetic accretor model for brevity, as they are extremely similar to Fig. 4), and the best-fitting parameters are again presented in Table 2. We also show examples of these model fits in Fig. 5; for ease of comparison, we show the same epochs as shown for the non-magnetic accretor model.

4 DISCUSSION

We have presented a multi-epoch spectral analysis of all of the broad-band data sets available for the bright ($L_{\rm X} \sim 10^{40}$ erg s^{-1}) ULX NGC 1313 X-1. These data sets combine observations taken with *XMM–Newton* and *Chandra* in coordination with *NuSTAR*, and span a period of $\sim$5 yr. The first of these epochs, XN1, corresponds to the data presented by Bachetti et al. (2013). From these observations we extracted nine broad-band spectra, covering the $\sim$0.5–30 keV energy range, which probe the spectral variability exhibited on time-scales of $\sim$days to $\sim$years (see Section 3). Several of these are broadly similar to epoch XN1 (epochs XN3, CN1, XN5, CN2), but others probe higher fluxes and show clear differences in their spectra (epochs XN2, XN4a,b, XN6; see Fig. 3).

In a qualitative sense, the spectral variability exhibited by these observations is remarkably similar to that seen in Holmberg IX X-1 (see fig. 1 in Walton et al. 2017). Strong variability is apparent at low energies (below $\sim$10 keV), with the spectra showing a more flat-topped profile at lower fluxes, and becoming more centrally peaked at higher fluxes. However, at higher energies the data pinch together and remain remarkably stable. Indeed, despite the factor of $>$3 variations seen at $\sim$3 keV, the 10–40 keV fluxes only vary by a factor of at most $\sim$1.5 (see Fig. 3). A similar effect may also have been seen at higher energies in the high-mass X-ray binary GX 301–2, which exhibited notable stability in the emission seen by *NuSTAR* above $\sim$40 keV despite clear variability at lower energies (Fürst et al. 2018).

As discussed previously, ULXs are now generally expected to represent a population of super-Eddington accretors, at least some of which are powered by neutron stars. We therefore construct spectral models that may broadly represent emission from a super-Eddington accretion flow. Such accretion flows are broadly expected to be formed of a large scale height inner funnel, a strong wind launched by this inner funnel (which may be optically thick) and a more standard thin outer accretion disc (which may be shrouded by the wind), so our models include two multicolour blackbody components with different temperatures, one for the inner funnel and one for the outer disc/wind. These dominate the observed spectra below $\sim$10 keV; in general, the cooler component contributes primarily below $\sim$1 keV, while the hotter component contributes primarily in the $\sim$1–10 keV band. Similar models have

Table 2. Best-fitting parameters from the nine broad-band spectra currently available for NGC 1313 X-1 for the models assuming a non-magnetic and a magnetic accretor, respectively.

Model Component	Parameter		Epoch XN1	XN2	XN3	XN4a	XN4b	CN1	XN5	CN2	XN6
Non-magnetic accretor model: TBABS× (DISKBB + DISKPBB ⊗ SIMPL)											
TBABS	$N_{\rm H,int}$ [a]	(10^{21} cm^{-2})	$2.47^{+0.05}_{-0.08}$	–	–	–	–	–	–	–	–
DISKBB	$T_{\rm in}$	(keV)	0.27 ± 0.01	$0.35^{+0.03}_{-0.02}$	0.30 ± 0.01	0.36 ± 0.02	0.33 ± 0.01	$0.16^{+0.07}_{-0.05}$	0.25 ± 0.01	$0.18^{+0.07}_{-0.06}$	0.32 ± 0.01
	Norm		$17.3^{+2.0}_{-2.3}$	$4.5^{+2.1}_{-1.6}$	$9.9^{+1.6}_{-1.4}$	$7.2^{+1.9}_{-2.1}$	$6.7^{+1.2}_{-1.0}$	160^{+2930}_{-140}	$21.8^{+2.7}_{-3.1}$	67^{+728}_{-58}	$8.9^{+2.7}_{-2.2}$
DISKPBB	$T_{\rm in}$	(keV)	$3.0^{+0.2}_{-0.3}$	$1.0^{+0.3}_{-0.1}$	$1.9^{+0.9}_{-0.5}$	$1.6^{+0.1}_{-0.2}$	$1.3^{+0.2}_{-0.1}$	3.1 ± 0.7	2.3 ± 0.4	$2.9^{+0.8}_{-1.0}$	$0.9^{+0.2}_{-0.1}$
	p		0.58 ± 0.01	$0.55^{+0.03}_{-0.01}$	$0.59^{+0.04}_{-0.02}$	$0.61^{+0.05}_{-0.03}$	$0.55^{+0.02}_{-0.01}$	0.57 ± 0.02	$0.62^{+0.03}_{-0.02}$	$0.57^{+0.03}_{-0.02}$	$0.59^{+0.05}_{-0.03}$
	Norm	(10^{-3})	$0.8^{+0.4}_{-0.2}$	50^{+66}_{-30}	$3.1^{+4.5}_{-1.8}$	28^{+26}_{-7}	13^{+12}_{-4}	$0.7^{+0.5}_{-0.4}$	$2.6^{+3.2}_{-1.3}$	$0.8^{+3.1}_{-0.5}$	96^{+165}_{-57}
SIMPL	Γ [a]		$2.94^{+0.07}_{-0.08}$	–	–	–	–	–	–	–	–
	$f_{\rm scat}$	(per cent)	21^{+8}_{-7}	>70	>32	35^{+10}_{-9}	>82	20^{+25}_{-9}	44^{+25}_{-18}	36^{+44}_{-23}	>70
χ^2/DoF			12 544/11 559								
Magnetic accretor model: TBABS× (DISKBB + DISKPBB + CUTOFFPL)											
TBABS	$N_{\rm H,int}$ [a]	(10^{21} cm^{-2})	$2.53^{+0.06}_{-0.07}$	–	–	–	–	–	–	–	–
DISKBB	$T_{\rm in}$	(keV)	0.27 ± 0.01	$0.38^{+0.04}_{-0.02}$	0.30 ± 0.01	0.36 ± 0.02	0.33 ± 0.01	$0.17^{+0.07}_{-0.06}$	0.25 ± 0.01	$0.18^{+0.08}_{-0.06}$	$0.34^{+0.02}_{-0.01}$
	Norm		$17.5^{+2.6}_{-2.1}$	$3.2^{+1.3}_{-1.1}$	$10.1^{+2.0}_{-1.8}$	$7.1^{+2.2}_{-2.0}$	$8.1^{+1.3}_{-1.1}$	120^{+2580}_{-110}	$22.6^{+3.3}_{-2.7}$	61^{+1039}_{-53}	$6.3^{+1.7}_{-1.5}$
DISKPBB	$T_{\rm in}$	(keV)	$2.9^{+0.2}_{-0.3}$	$1.6^{+0.2}_{-0.1}$	$2.0^{+0.4}_{-0.3}$	1.7 ± 0.1	1.5 ± 0.1	$2.6^{+0.9}_{-0.5}$	$2.2^{+0.4}_{-0.2}$	$2.5^{+0.7}_{-0.5}$	1.5 ± 0.1
	p		0.56 ± 0.01	$0.54^{+0.01}_{-0.02}$	$0.57^{+0.06}_{-0.03}$	0.60 ± 0.03	$0.55^{+0.03}_{-0.01}$	$0.55^{+0.04}_{-0.02}$	$0.60^{+0.03}_{-0.02}$	$0.55^{+0.05}_{-0.02}$	0.56 ± 0.03
	Norm	(10^{-3})	$0.7^{+0.3}_{-0.2}$	$9.3^{+4.5}_{-3.3}$	$2.3^{+2.8}_{-1.4}$	$18.0^{+8.8}_{-5.8}$	$10.8^{+5.1}_{-3.5}$	$1.0^{+1.6}_{-0.6}$	$2.1^{+1.2}_{-1.0}$	$1.0^{+1.7}_{-0.6}$	$13.8^{+5.4}_{-3.9}$
CUTOFFPL	Γ		0.59 [b]	–	–	–	–	–	–	–	–
	$E_{\rm fold}$	(keV)	7.1 [b]	–	–	–	–	–	–	–	–
	$F^{\rm cpl}_{2-10}$ [c]	(10^{-13} erg cm^{-2} s^{-1})	$5.3^{+1.0}_{-1.4}$	$8.5^{+0.9}_{-1.1}$	$7.9^{+0.9}_{-1.5}$	$10.3^{+1.5}_{-1.8}$	$11.3^{+0.8}_{-1.0}$	$7.0^{+1.9}_{-5.3}$	$7.2^{+1.2}_{-2.3}$	$8.1^{+1.5}_{-3.4}$	8.2 ± 0.7
χ^2/DoF			12 572/11 560								
$F^{\rm obs}_{0.3-40.0}$ [d]	(10^{-13} erg cm^{-2} s^{-1})		42.2 ± 0.7	$59.9^{+1.9}_{-2.0}$	$38.7^{+1.2}_{-1.3}$	$87.2^{+3.1}_{-3.2}$	$55.6^{+2.0}_{-1.9}$	$41.4^{+2.0}_{-1.9}$	$38.7^{+1.3}_{-1.4}$	39.1 ± 1.7	57.7 ± 1.6
$F^{\rm obs}_{0.3-1.0}$ [d]			4.1 ± 0.1	6.1 ± 0.2	$3.7^{+0.2}_{-0.1}$	7.6 ± 0.3	5.5 ± 0.2	$3.6^{+0.7}_{-1.2}$	$3.6^{+0.1}_{-0.2}$	$3.1^{+0.9}_{-0.7}$	6.1 ± 0.2
$F^{\rm obs}_{1.0-10.0}$ [d]			29.9 ± 0.5	45.3 ± 1.5	$26.8^{+0.9}_{-0.8}$	$68.5^{+2.4}_{-2.5}$	$39.4^{+1.5}_{-1.4}$	$29.1^{+1.0}_{-1.1}$	27.0 ± 0.9	$26.9^{+0.9}_{-1.0}$	43.5 ± 1.2
$F^{\rm obs}_{10.0-40.0}$ [d]			8.1 ± 0.4	$8.5^{+0.7}_{-0.8}$	$8.1^{+0.5}_{-0.7}$	$11.1^{+1.1}_{-1.2}$	$10.7^{+0.7}_{-0.8}$	$8.8^{+0.9}_{-1.1}$	$8.1^{+0.7}_{-0.9}$	$9.2^{+0.7}_{-1.0}$	$8.1^{+0.5}_{-0.6}$
$L^{\rm int}_{0.3-40.0}$ [e]	(10^{39} erg s^{-1})		$12.3^{+0.2}_{-0.3}$	$17.6^{+0.5}_{-0.6}$	$11.2^{+0.3}_{-0.4}$	$24.4^{+0.8}_{-0.9}$	$16.2^{+0.5}_{-0.6}$	$12.3^{+2.9}_{-1.5}$	$11.2^{+0.3}_{-0.4}$	$11.1^{+1.9}_{-1.1}$	$17.0^{+0.4}_{-0.5}$

Notes. [a]These parameters are globally free to vary, but are linked across all epochs.
[b]These parameters are fixed to the average values seen from the pulsed emission from the currently known ULX pulsars, and are common for all epochs.
[c]The observed flux from the CUTOFFPL component associated with the potential accretion column in the 2–10 keV band.
[d]The total observed flux in the full 0.3–40.0 keV band, and the 0.3–1.0, 1.0–10.0, and 10.0–40.0 keV sub-bands, respectively (consistent for both models).
[e]Absorption-corrected luminosity in the full 0.3–40.0 keV band (consistent for both models). These values assume isotropic emission, and may therefore be upper limits (see Section 4).

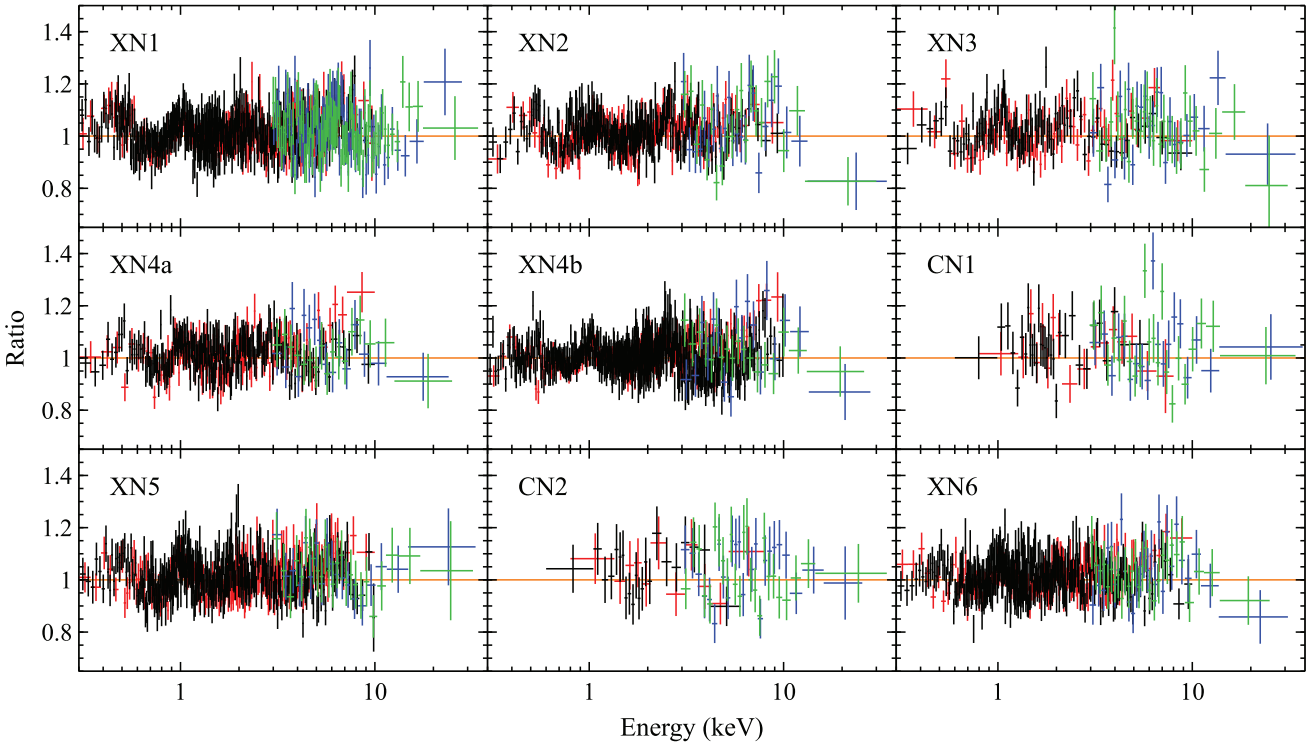

Figure 4. Data/model ratios for the nine broad-band spectra extracted of NGC 1313 X-1 fit with the model assuming a non-magnetic accretor. Green and blue show data from the *NuSTAR* FPMA and FPMB detectors, respectively, while black and red show data from the EPIC-pn and EPIC-MOS detectors, respectively, for the XN epochs and from the MEG and HEG gratings, respectively, for the CN epochs. As with Fig. 3, the data have been further rebinned for display purposes. The data/model ratios for the model assuming a magnetic accretor are extremely similar to those shown here.

frequently been applied to ULX data below 10 keV (e.g. Stobbart et al. 2006; Gladstone et al. 2009; Walton et al. 2014). In the case of NGC 1313 X-1, the need for two components below 10 keV is visually apparent for the lower flux observations (Fig. 3). However, even for the higher flux epochs, where this is not as obvious, the spectral decomposition found here is supported by the short-time-scale variability results presented by Kara et al. (2020) for epoch XN4 (the most variable broad-band epoch). The covariance analysis presented in that work clearly shows evidence for distinct spectral components above and below ∼2 keV (see also Middleton et al. 2015a), similar to the model used here.

However, as demonstrated by Walton et al. (2018c), when fit with such models all ULXs observed by *NuSTAR* to date (including NGC 1313 X-1) require an additional component at high energies to account for the *NuSTAR* data above ∼10 keV, as the Wien tail in accretion disc models falls off too steeply. Since pulsations have not currently been observed from NGC 1313 X-1, and so the nature of the accretor in this system is not currently known, we take two different approaches to modelling this additional high-energy component. First, we treat it as a high-energy power-law tail produced by Compton up-scattering in an X-ray corona, similar to that seen in other X-ray binary systems. We refer to this as the non-magnetic scenario, which may be appropriate for both black hole and non-magnetic neutron star accretors. Secondly, we treat it as high-energy emission from a super-Eddington accretion column on to a magnetized neutron star, and assume a spectral form motivated by the pulsed emission observed from the known ULX pulsars (using the average spectral shape of their pulsed spectra as a template). We refer to this as the magnetic scenario.

Walton et al. (2017) suggested that the broad-band spectral variability seen in Holmberg IX X-1, similar to that reported here for NGC 1313 X-1, could potentially be related to the presence of the expected funnel-like geometry for the inner accretion flow. In such a scenario, the funnel is expected to geometrically collimate the emission from the innermost regions within the funnel (discussed further in Section 4.2). Regardless of the nature of the accretor (black hole or neutron star), the highest energy emission probed by *NuSTAR* is usually expected to arise from these regions, either powered by a centrally located Compton-scattering corona (e.g. Reis & Miller 2013), or a centrally located accretion column. The stability of this emission would therefore imply that any geometrical collimation it experiences remains roughly constant, despite the change in observed broad-band X-ray flux (which would suggest a change in accretion rate, $\dot{M}$). In principle, an increase in accretion rate would be expected to result in an increase in the scale height of the funnel (e.g. King 2008; Middleton et al. 2015a). However, while this must happen over some range of $\dot{M}$ in order for the disc structure to transition from the thin disc expected for standard sub-Eddington accretion to the funnel-like geometry expected for super-Eddington accretion, as discussed by Lasota et al. (2016), once the disc reaches the point of being fully advection-dominated the opening angle of the disc should tend to a constant ($H/R \sim 1$, where H is the scale height of the disc at radius R). Walton et al. (2017) speculated that once this occurs, rather than closing the funnel further, an increase in $\dot{M}$ instead simply increases the characteristic radius within which geometric beaming occurs, such that emission that is already within this region (the highest energies probed) experiences no further collimation with an increase in $\dot{M}$, while emission from larger radii (i.e. from more intermediate energies) does still become

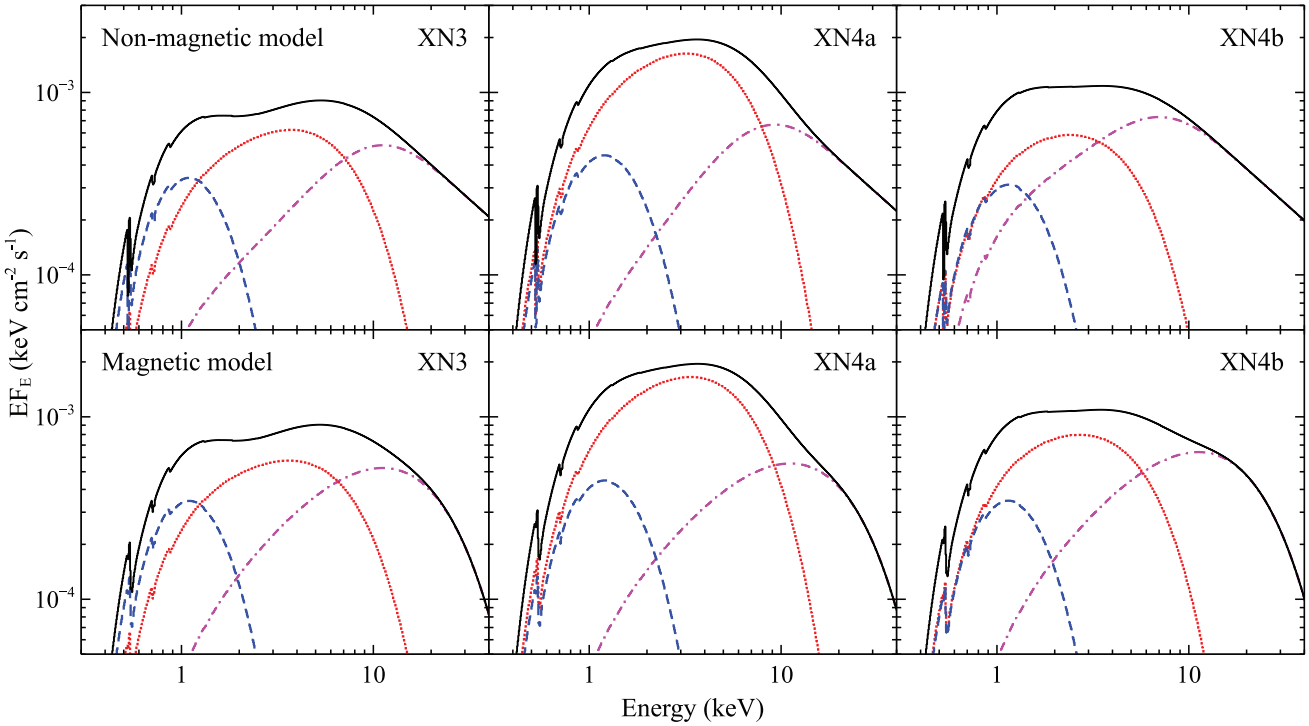

Figure 5. Example model fits for the non-magnetic accretor (top panels) and the magnetic accretor (bottom panels) models. We show the fits for epochs XN3 (representing the low-flux end of the broad-band spectra; left-hand panels), XN4a (the high-flux end of the broad-band spectra, middle panels), and XN4b (one of the intermediate flux spectra; right-hand panels). For both models, the total model is shown in solid black, the cooler DISKBB and the hotter DISKPBB components are shown in dashed blue and dotted red, respectively (in the black hole case, the DISKPBB component is shown as it would appear prior to the application of the SIMPL convolution model), and the highest energy component (either SIMPL or CUTOFFPL) is shown in dash–dotted magenta. For the non-magnetic model, the contribution from SIMPL has been calculated by subtracting the unmodified DISKPBB component from the combined SIMPL⊗DISKPBB contribution to the fit.

progressively more focused, and would exhibit stronger variability. In essence, this idea invokes a radially dependent beaming factor in which the beaming of the innermost regions has saturated to explain (in only a qualitative sense) the unusual, energy-dependent broad-band spectral evolution seen from Holmberg IX X-I (and now NGC 1313 X-1).

4.1 Evolution of the thermal components

With this picture in mind, and with a fairly extensive, broad-band data set now available for NGC 1313 X-1, we consider the behaviour of the two thermal components in each of our models in detail. In particular, we investigate how the DISKBB and DISKPBB components evolve in the luminosity–temperature plane. To compute the luminosity, we calculate the intrinsic fluxes (i.e. absorption corrected, and in the case of the DISKPBB component for the black hole model, corrected for the photons lost to the power-law tail) for each of the thermal components individually, computed over a broad enough band to be considered bolometric (0.001–100 keV). The results for each component are shown in Fig. 6 for both of the models considered.

We do not find any clear relationship between L and T for the lower temperature DISKBB component. However, this is likely related, at least in part, to our treatment of the hotter component with the DISKPBB model. This extends the run of temperatures down to arbitrarily low values, which is not physically reasonable if the two thermal components do represent radially distinct regions of the disc. This extrapolation will naturally influence the flux of the cooler DISKBB component, and could certainly serve to artificially mask any such relation, so the results presented here are not particularly well suited for addressing this issue for the cooler component. Indeed, based on archival *XMM–Newton* data, we note that Miller et al. (2013) find evidence for a positive relation between luminosity and temperature for the cooler DISKBB component when treating the higher energy emission with a Comptonization model,[1] and assuming that the seed photons come from the DISKBB component (such that this emission has a low-energy cut-off at the DISKBB temperature). Miller et al. (2013) may therefore present a more accurate assessment of the evolution of this cooler thermal component. This issue will be explored further in future work.

The most interesting results are instead seen for the hotter DISKPBB component. In both cases (the models for non-magnetic and magnetic accretors) the results cluster into two groups, split by the observed flux. The higher flux cases ($F^{\rm obs}_{0.3-40.0} > 5 \times 10^{-12}$ erg cm^{-2} s^{-1}; epochs XN2, XN4a,b, XN6) show lower temperatures on average, while the lower flux cases ($F^{\rm obs}_{0.3-40.0} < 5 \times 10^{-12}$ erg cm^{-2} s^{-1}; epochs XN1, XN3, XN5, CN1, CN2) show higher temperatures. Naively, one could conclude that luminosity and temperature are inversely correlated for this component, as also discussed for Holmberg IX X-1 by Walton et al. (2014). However,

[1]Owing to the lack of available *NuSTAR* data, only the 0.3–10.0 keV energy range covered by *XMM–Newton* was considered by Miller et al. (2013). As such, the energies dominated by the Comptonized emission in that case correspond to the intermediate energies dominated by the DISKPBB component here.

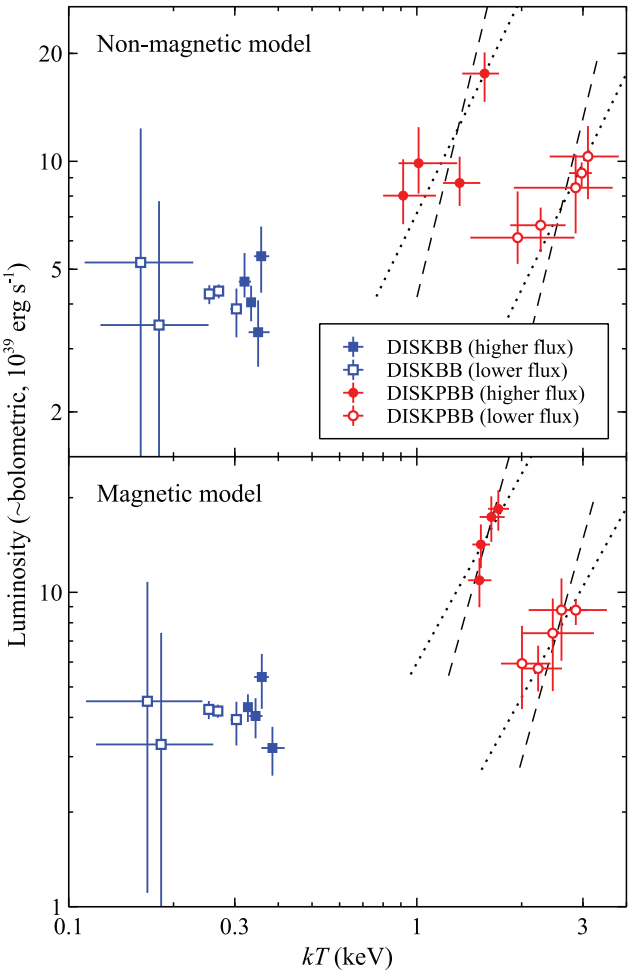

Figure 6. 0.001–100 keV (i.e. ∼bolometric) luminosity versus temperature for both the DISKBB (blue squares) and DISKPBB (red circles) components from our multi-epoch spectral analysis with the models assuming the accretor is non-magnetic (top) and magnetic (bottom). No clear relation is seen for the DISKBB component (although this may be related to modelling issues, see Section 4). However, in both cases the results for the DISKPBB component appear to show distinct tracks at high and low luminosities (observed fluxes above and below $F^{\rm obs}_{0.3-40.0} = 5 \times 10^{-12}$ erg cm^{-2} s^{-1}; full and open symbols, respectively), both of which are broadly consistent with $L \propto T^4$ (indicated with the dashed lines), and also with $L \propto T^2$ (dotted lines).

Table 3. Pearson's correlation coefficients and null hypothesis probabilities (no correlation) for the low- and high-temperature tracks for the DISKPBB component seen in Fig. 6 for the non-magnetic and the magnetic accretor models.

Model	Low temp.		High temp.	
	ρ	$p_{\rm null}$	ρ	$p_{\rm null}$
Non-magnetic accretor	0.77	0.23	0.97	0.005
Magnetic accretor	0.87	0.13	0.91	0.03

when considered separately, each of these groups appear to exhibit a positive correlation (see Fig. 6). We present Pearson's correlation coefficients (ρ) and null hypothesis probabilities (i.e. the probability of no correlation; $p_{\rm null}$) in Table 3. Although the data are visually compelling, the formal statistical evidence for a correlation is not as strong for the higher luminosity/lower temperature group, in large part because this group is only made up of four epochs (although we note that for the non-magnetic accretor model, the evidence for a correlation is driven purely by epoch XN4a). Ultimately, further observational data will be required to robustly confirm this behaviour.

Nevertheless, each of the two groups of observations are broadly consistent with following their own distinct $L \propto T^4$ relationship, which would be expected for blackbody radiation with a constant emitting area. Although the qualitative results regarding e.g. temperature do depend on the choice of model, and the global uncertainties are larger in the black hole model because the shape of the high-energy continuum is free to vary in this case, qualitatively this behaviour appears to be largely model independent, as it is seen for both of the models considered. We have also performed a series of other tests related to the models used, including allowing the neutral absorption column to vary between epochs (following Middleton et al. 2015a), replacing the cooler DISKBB component with a single-temperature blackbody and linking p across all of the data sets in the magnetic model, and allowing for different photon indices for the two groups of observations in the non-magnetic model. We still see qualitatively consistent behaviour in the hotter DISKPBB component to that shown above in all of these cases. In addition, we also further tested whether the spectral variability inferred for the DISKPBB component within each group of observations is really required by the data, as this drives the two positive luminosity–temperature correlations seen in Fig. 6. To do so we re-fit the data assuming common values for both p and $T_{\rm in}$ for the DISKPBB component for the observations that make up each group, allowing only for the flux of this component to vary within them. This significantly degrades the fit by $\Delta\chi^2 \sim 100$ (for 14 fewer free parameters) for both the non-magnetic and the magnetic accretor models; F-tests imply the probabilities of these differences in fit statistic occurring by chance are $\sim 10^{-12}$ in both cases.

Given the concerns regarding the extrapolation of the DISKPBB model mentioned above, we also investigated whether the results for this component shown in Fig. 6 could be influenced by extending this component significantly outside of the observed bandpass. Instead of using the broader 0.001–100 keV fluxes shown in Fig. 6, we also compute the fluxes for this model component above 1 keV, which is primarily covered by the observed bandpass. Although the quantitative details naturally change, the same qualitative behaviour is still seen: the observations split into two distinct groups with their own luminosity–temperature tracks, each of which are consistent with $L \propto T^4$. In the non-magnetic case the results for this higher energy band are again not as clear-cut as the magnetic case, but the data are also still consistent with there being two groups following separate tracks, each again consistent with $L \propto T^4$. The observed behaviour therefore appears to be largely robust to any issues regarding extrapolation of the DISKPBB component outside of the observed bandpass. We also note that this demonstrates that the atomic features associated with the wind, which are not modelled here, do not significantly influence the observed luminosity–temperature behaviour for the DISKPBB component, as these features have a very small effect on the DISKPBB flux above 1 keV (at the level of a few per cent; Pinto et al. 2020).

Owing to the small number of observations and the relatively limited dynamic range currently available for each track, we do not fit for formal luminosity–temperature relations at this stage. Instead, to test for the consistency with $L \propto T^4$ in a simple manner, we perform some further fits to the data in which we assume constant inner radii ($R_{\rm in}$) for the DISKPBB component for each of the two groups of observations. Formally we link their normalizations,

which are given by $[R_{\rm in}/(\xi D f_{\rm col}^2)]^2 \cos(i)$, where $R_{\rm in}$ and D are in units of km and 10 kpc, respectively, i is the inclination of the disc, $f_{\rm col}$ is its colour correction factor, and ξ is a further correction introduced by the inner boundary condition assumed in the DISKBB/DISKPBB models ($\xi \sim 0.4$; Kubota et al. 1998; Vierdayanti, Watarai & Mineshige 2008). The colour correction factor is a simple multiplicative correction designed to empirically account for the complex atmospheric physics in the disc by relating its 'colour' temperature at the photosphere ($T_{\rm col}$) to its effective blackbody temperature ($T_{\rm eff}$), and is defined as $T_{\rm col} = f_{\rm col} T_{\rm eff}$. Assuming that i and $f_{\rm col}$ are similar for the DISKPBB component for both groups of observations, the ratio of their inner radii is simply related to the ratio of their normalizations, i.e. $R_{\rm in,1}/R_{\rm in,2} = \sqrt{{\rm Norm}_1/{\rm Norm}_2}$ (where subscripts 1 and 2 refer to the lower and higher temperature tracks, respectively). Although we now have seven fewer free parameters, these fits are only worse by $\Delta\chi^2 = 21$ and 15 for the non-magnetic and magnetic models, respectively, and we find that the ratios of the two radii are $R_{\rm in,1}/R_{\rm in,2} = 4.6^{+1.2}_{-1.0}$ and $3.6^{+0.6}_{-0.7}$.

We also estimate the minimum inner radii (in the context of isotropic emission) for the DISKPBB component implied by the two potential $L \propto T^4$ tracks by assuming no colour correction (i.e. $f_{\rm col} = 1$) and a face-on inclination (i.e. $i = 0$). For the non-magnetic model, these inner radii are $R_{\rm in,1} \sim 26$ km and $R_{\rm in,2} \sim 5.6$ km, while for the magnetic model these inner radii are $R_{\rm in,1} \sim 19$ km and $R_{\rm in,2} \sim 5.2$ km. We stress that any colour correction and/or non-zero inclination will increase these estimates. Although the colour correction is typically taken to be $f_{\rm col} = 1.7$ for sub-Eddington accretion (e.g. Shimura & Takahara 1995), for super-Eddington accretion $f_{\rm col} \sim 3$ may be more appropriate (Watarai & Mineshige 2003, Davis & El-Abd 2019, and in reality $f_{\rm col}$ may have a radial dependence, Soria, Wu & Kunic 2008). Adopting this value and an inclination of $i = 60^\circ$, for example, increases these estimates by a factor of $3^2/\sqrt{0.5} \approx 12.7$ to $R_{\rm in,1} \sim 320$ km and $R_{\rm in,2} \sim 71$ km for the non-magnetic model, and to $R_{\rm in,1} \sim 240$ km and $R_{\rm in,2} \sim 66$ km for the magnetic model. If the accretor is a 10 $M_\odot$ black hole, these radii would correspond to $R_{\rm in,1} \sim 20\,R_{\rm G}$ (where $R_{\rm G} = GM/c^2$ is the gravitational radius) and $R_{\rm in,2} \sim 5\,R_{\rm G}$, and if the accretor is a $\sim$1.4 $M_\odot$ neutron star they would correspond to $R_{\rm in,1} \sim 115-150\,R_{\rm G}$ and $R_{\rm in,2} \sim 30\,R_{\rm G}$. In this latter case (1.4 $M_\odot$ neutron star), the radii inferred are vaguely similar to the launching radii for the two main components of the wind inferred by Pinto et al. (2020), based on escape velocity arguments ($\sim$50 and $\sim$300 $R_{\rm G}$, i.e. within a factor of $\sim$2). In the former (10 $M_\odot$ black hole), all of the changes inferred here would appear to be occurring interior to the wind launching regions based on the same arguments, although the larger radius is similarly comparable to the innermost radius for the wind (again within a factor of $\sim$2).

It is important to note that the two groups of observations that show these different $L \propto T^4$ tracks do not simply represent distinct periods of time over which these different emitting radii remained stable. Instead, the source appears to switch back-and-forth between them. The cadence of our broad-band sampling is not particularly constraining with regards to the transition between these two tracks; from these data we can only determine that NGC 1313 X-1 is able to move between them in the space of a few weeks (the time between epochs XN4 and CN1). Should these two tracks represent intrinsic evolution in the DISKPBB component, these two radii would therefore imply that there are two stable geometric configurations that NGC 1313 X-1 repeatedly returns to/transitions between. It is also important to note that the epochs exhibiting higher observed luminosities also show the larger of the two radii. This makes it unlikely the observed behaviour is related to bulk precession of an otherwise stable (i.e. constant accretion rate) large scale-height inner flow changing our ability to view the emission from its innermost regions (e.g. Middleton et al. 2018). In this scenario, the smaller inner disc radii should be observed when we can see further into the funnel, and therefore be associated with higher observed fluxes. Furthermore, there is no hint that the long-term variability exhibited by NGC 1313 X-1 is even quasi-periodic (Fig. 1), instead exhibiting a marked increase in seemingly aperiodic variability after MJD $\sim$ 57400 (as noted previously).

Given the presence of the two luminosity–temperature tracks, we also explore the possibility that there are actually two distinct thermal components (each producing one track) that are always present and, in combination, dominate the $\sim$1–10 keV band (such that the $\sim$0.3–40 keV spectrum would actually be made up of four continuum components, instead of the three used in our previous modelling). This might, for example, represent a scenario in which there is even further radial segregation of the accretion flow than included in our baseline models (see Section 4.5 for further discussion). In this picture, these two thermal components exhibit different levels of long-term variability, such that their relative contribution changes from epoch to epoch, and in our three-component models the DISKPBB component is forced to (and has sufficient flexibility to) primarily account for whichever of these two components dominates the $\sim$1–10 keV band for any particular epoch, switching its apparent properties between the two as necessary. For brevity and simplicity, we focus on the magnetized accretor model and replace the DISKPBB component with two standard DISKBB accretion disc models, each of which has a normalization linked across all the epochs considered (i.e. we assume each new DISKBB component varies following $L \propto T^4$). As such, the full continuum model in this case consists of three DISKBB components and the CUTOFFPL component associated with the accretion column. This actually provides a reasonable improvement to the fit obtained with the three-component model, with $\chi^2/{\rm DoF} = 12\,454/11\,567$ (i.e. $\Delta\chi^2 = 118$ for seven additional free parameters); the temperatures of the two new DISKBB components vary from $kT_1 \sim 0.6-1.0$ keV and from $kT_2 \sim 1.9-2.5$ keV, respectively. In this case, the ratio of the inner radii of the two new DISKBB components is $R_{\rm in,1}/R_{\rm in,2} = 6.4 \pm 0.6$, and the minimum possible inner radii (again assuming no colour correction and a face-on inclination) inferred are $R_{\rm in,1} \sim 75$ km and $R_{\rm in,2} \sim 12$ km. We stress that these radii should be taken with a large degree of caution, as the issues regarding extrapolation of the individual thermal models to low energies discussed above are even further exacerbated in this case; the values are primarily presented for completeness and reproducibility.

Although the luminosity–temperature tracks returned by our analyses are consistent with $L \propto T^4$, in most cases they are also consistent with flatter luminosity–temperature relations. In particular, most tracks are also consistent with $L \propto T^2$ (also shown in Fig. 6), which, even if $R_{\rm in}$ remains $\sim$constant, may be expected for the inner regions of an advection-dominated disc around a black hole (in which some of the radiated flux from these regions is trapped by the flow and carried across the event horizon, e.g. Watarai et al. 2000; note that this is not possible for a neutron star accretor, as in that case the radiation must emerge in some form). Some Galactic black hole X-ray binaries are seen to transition to a luminosity–temperature relation similar to $L \propto T^2$ at high luminosities (see *e.g.* Kubota & Makishima 2004; Abe et al. 2005), and some ULXs also show evidence for this behaviour (Walton et al. 2013). Similar to the $L \propto T^4$ case, we perform additional fits where the normalizations of the DISKPBB component are linked across each of the two groups of observations in a manner that would give $L \propto T^2$; again with

seven fewer free parameters, we find the fits are only worse by $\Delta\chi^2 = 31$ and 30 for the non-magnetic and magnetic models, respectively. The global fits are therefore marginally worse than (but still essentially comparable to) the fits assuming $L \propto T^4$. Given the limited dynamic range covered by each of the tracks, the radii estimated above assuming $L \propto T^4$ are likely still representative of the characteristic emitting radii that would be inferred for each of the two groups of observations even if $L \propto T^2$. However, since in this case the 'true' disc luminosity is underestimated (as some fraction is advected over the horizon), the absolute radii would likely be underestimated (see e.g. Kubota & Makishima 2004).

In the following sections, we discuss potential physical causes for the two distinct luminosity–temperature tracks associated with the DISKPBB component, and also explore potential scenarios in which stable emitting radii could be produced in the accretion flow for NGC 1313 X-1.

4.2 Geometric collimation and disc/wind scale height

The above estimates for the emitting radii do not account for any geometric collimation of the radiation that might be experienced by the emission from these thermal components. As discussed previously, this may be expected for the inner regions of a super-Eddington accretion flow, which, through the combination of the outer disc and the wind, should form a funnel-like geometry. Should any of the thermal emission arise from regions interior to this inner funnel then it should be collimated into a solid angle set by the opening angle of this funnel, Ω. By assuming no collimation, the total luminosity emitted and in turn the emitting radii would be overestimated. Introducing a 'beaming' factor of $b = \Omega/4\pi$, such that the 'observed' luminosity inferred assuming isotropic emission, $L_{\rm obs}$, and the actual emitted luminosity, $L_{\rm int}$, are related via $L_{\rm int} = bL_{\rm obs}$ (following King 2008, such that $b \leq 1$; we assume here that we are looking down the funnel), then should any of the thermal emission be collimated the radii inferred from this emission would need to be corrected by a factor $\sqrt{b}$.

Furthermore, any variations in the degree of beaming b would manifest as changes in the emitting areas/radii in our analysis. Indeed, if we consider the case where there is more collimation of a blackbody thermal component at higher intrinsic luminosities, as may be expected for a disc which has a larger scale height at higher accretion rates, we can write $b \propto L_{\rm int}^{-\beta}$, where $\beta > 0$ (as more collimation corresponds to smaller b in our definition). Assuming that the intrinsic emission behaves as $L_{\rm int} \propto T^{\alpha}$, and that the process of collimation does not also change T (i.e. $T_{\rm int} = T_{\rm obs} = T$; this will be discussed further in Section 4.4), combining this with the definition of b and the scaling between b and $L_{\rm int}$ we find that $L_{\rm obs} \propto T^{\alpha(1+\beta)}$. Non negligible β could therefore produce clear deviations from $L_{\rm obs} \propto T^4$ for a constant area blackbody, with a steeper luminosity–temperature scaling expected in this particular scenario.[2] If both $L_{\rm obs} \propto T^4$ and $L_{\rm int} \propto T^4$, or both $L_{\rm obs} \propto T^2$ and $L_{\rm int} \propto T^2$, then b must be constant. Alternatively, it would still be possible to produce $L_{\rm obs} \propto T^4$ even if $L_{\rm int} \propto T^2$ provided that $b \propto L_{\rm int}^{-1}$. However, in any of these cases, in order to produce two distinct groups in the luminosity–temperature plane purely through beaming, there would need to be a sharp transition in b at some point. This is naturally problematic for any model invoking progressive changes in the opening angle of a large scale height inner flow. In addition to being problematic for models invoking progressive changes in the scale height of the disc, it is similarly unclear how the picture of a progressively changing radial beaming profile suggested by Walton et al. (2017) for Holmberg IX X-1 would be able to explain the two distinct groups of observations seen for NGC 1313 X-1.

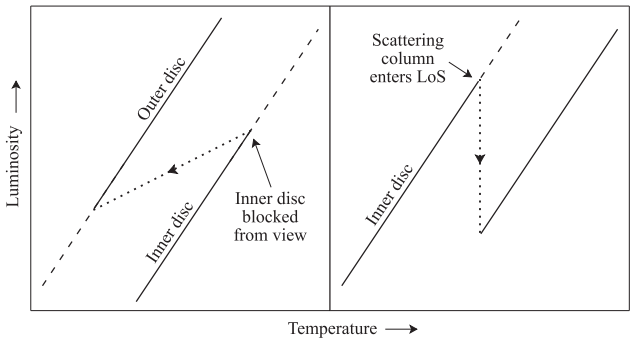

Figure 7. Toy models for the luminosity–temperature plane for the scenarios in which the inner disc is suddenly fully obscured by the outer disc/wind (left-hand panel; discussed in Section 4.2) and in which the emission from the inner disc is scattered by a highly ionized wind which still permits some of the emission to escape (right-hand panel; discussed in Section 4.3).

A model invoking a larger scale height at higher accretion rates could instead potentially produce a sharp transition in the luminosity–temperature plane should our viewing angle be close to the opening angle of the flow at lower luminosities, such that by increasing the scale height of the disc/wind the innermost regions of the flow are suddenly obscured by the regions at larger radii, resulting in a larger inner radius being inferred at higher luminosities.[3] For this to be a plausible explanation for the broad-band behaviour, the obscuring regions would need to correspond to those contributing the lower temperature parts of the DISKPBB component that are still visible in the higher flux observations. A toy model for the transition in the luminosity–temperature plane in this scenario is shown in Fig. 7 (left). However, if the thermal emission from the inner regions of the disc is suddenly obscured, one would naturally expect a central corona/accretion column to be similarly obscured, but the high-energy *NuSTAR* data are rather stable.

4.3 Scattering losses in a wind

Alternatively, it may be the case that the high-temperature track is actually a smooth continuation of the low-temperature track, but that above some observed luminosity we view the emission through an ionized disc wind, which results in an apparent decrease in the

[2]Note that this differs from the scaling discussed by King (2009) who, with similar assumptions (i.e. increased beaming at higher accretion rates and no change in T), suggest that increasingly beamed blackbody emission (intrinsically emitting as $L_{\rm int} \propto T^4$) could result in $L_{\rm obs} \propto T^{-4}$. However, this essentially assumes that the ratio $l = L_{\rm int}/L_{\rm E}$ remains constant, as in the full expression derived $L_{\rm obs} \propto l^2/(T^4 r^2 b)$ (where r is the emitting radius in units of Schwarzschild radii). This ratio is clearly not constant here (as $L_{\rm int}$ must vary), meaning that the right-hand-side still has further temperature dependencies that need to be accounted for (as $L_{\rm int} \propto T^4$). Substituting l for T, and again assuming that $b \propto L_{\rm int}^{-\beta}$, we return to the $L_{\rm obs} \propto T^{4(1+\beta)}$ dependence derived here.

[3]Here we assume that the inner regions are fully obscured, such that none of the emission from these regions is visible to us.

observed flux due to losses associated with electron scattering.[4] A toy model for the transition in the luminosity–temperature plane in this scenario is also shown in Fig. 7 (right). Indeed, NGC 1313 X-1 is now known to launch a powerful disc wind (Middleton et al. 2015b; Pinto et al. 2016, 2020), which at least at times has a highly ionized component along our line of sight (Walton et al. 2016a). To test this scenario, we perform some further fits in which we assume a single normalization for the DISKPBB nent for all epochs, and apply a CABS component to this emission for the observations that make up the higher temperature track, again focusing on the magnetic accretor model for brevity. CABS accounts for flux losses due to electron scattering, and is characterized by an effective column density for the scattering medium, which we link across the high-temperature observations in order to preserve a common intrinsic $L_{\rm obs} \propto T^4$ scaling for both the high- and low-temperature tracks. We find that this provides an equivalently good fit to the model with two linked DISKPBB normalizations (see Section 4.1), with χ^2/DoF = 12604/11567, and that the scattering column density required to bring about the drop in flux inferred from an extrapolation of the low-temperature track to the observed high-temperature track is $N_{\rm H} = 3.1^{+0.3}_{-0.4} \times 10^{24}$ cm^{-2}.

The scattering column required is significantly larger than the best-fitting column densities inferred for any of the components of the wind in NGC 1313 X-1 reported to date. For the moderately ionized components that contribute the features detected at ∼1 keV by the RGS, $N_{\rm H} \sim 10^{21-22}$ cm^{-2} (Pinto et al. 2016, 2020).[5] For the highly ionized component that provides the iron K absorption seen in archival *XMM–Newton* and *NuSTAR* data (which are primarily made up of epoch XN1), $N_{\rm H} \sim 10^{23}$ cm^{-2} (Walton et al. 2016a), although it is worth noting that there is a local minimum in the parameter space for the highly ionized component that does extend up to column densities comparable to that inferred above ($N_{\rm H} \sim 10^{24}$ cm^{-2}). Fixing the CABS column density to 10^{23} cm^{-2} in this scenario significantly degrades the fit ($\Delta\chi^2 = 165$ for one fewer free parameter, giving a negligible *F*-test probability of a chance improvement), as the scattering losses are very small; the CABS component is therefore unable to reproduce the required drop in flux, and the model instead tries to produce this drop by introducing large differences in p for the two groups, resulting in a notably worse fit.

As noted above, this scenario would require there to be a sharp transition in the wind properties along our line of sight to explain the observed behaviour. Furthermore, if both tracks follow $L_{\rm obs} \propto T^4$, or both follow $L_{\rm obs} \propto T^2$, then the wind properties would need to be bi-modal, such that we are either viewing the central regions through a negligible scattering column, or through basically the same column whenever our line of sight intercepts the wind. Although Middleton et al. (2015b) do find that the residuals at ∼1 keV imprinted by the wind are weaker in archival *XMM–Newton* observations that would lie on the higher flux, lower temperature track, the evolution appears to be a continuous function of the observed hardness of the source. Indeed, Pinto et al. (2020) find that, although there are some differences in the properties of the wind between observations in the two tracks, both still show broadly similar absorption from the moderately ionized components in the RGS data. In order for this scenario to be plausible, the local minimum at $N_{\rm H} \sim 10^{24}$ cm^{-2} reported in Walton et al. (2016a) would likely need to be the correct solution, and this highly ionized component would also need to show much stronger variability between the two tracks than these more moderately ionized components. The work so far on the wind properties in the new 2017 campaign has focused on the RGS band, and is not particularly sensitive to the highly ionized component that would be most relevant for this scenario (the current absorption analysis does not exclude this scenario, Pinto et al. 2020); this will be further addressed in future work. Alternatively, it could be that the scattering medium is a fully ionized component of the wind, such that it does not imprint any discernible absorption features. However, fully ionizing a column of $N_{\rm H} \sim 3 \times 10^{24}$ cm^{-2} such that there is no significant absorption opacity below 10 keV is obviously challenging, particularly if the DISKBB temperature (∼0.2–0.4 keV) represents the characteristic temperature of the wind. Regardless, as with the scenario in which the outer disc fully blocks the inner disc, it is similarly difficult to explain the lack of strong long-term variability at the highest energies in this scenario under the assumption that this emission comes from the most compact regions.

4.4 The colour correction factor and down-scattering

Beyond geometric considerations, which all have difficulty explaining the stability of the highest energy emission, it may also be possible to produce two apparently distinct luminosity–temperature tracks by varying the colour correction factor, $f_{\rm col}$, introduced by the atmosphere of the disc (previously we assumed a single value for all of the available data). However, similar to the above cases, in order to do so $f_{\rm col}$ would need to have two distinct values that it varies between, or at the very least exhibit a sharp jump at some point in its evolution with accretion rate. This would result in a sudden change in the observed temperature at a given luminosity. However, none of the works that have tried to consider how this should vary with accretion rate have shown an obvious indication for such a sudden jump (Shimura & Takahara 1995; Davis & El-Abd 2019). Furthermore, the general expectation among these works is that $f_{\rm col}$ should increase with increasing accretion rate, which should result in the highest temperatures being observed at the highest luminosities. Again, this is not the case, so it is not clear that this is a realistic possibility either.

In addition to the atmospheric corrections associated with the disc, if the emission from the inner regions is geometrically collimated by the outer disc/wind, the cooler temperatures associated with these regions could result in significant down-scattering (e.g. Middleton et al. 2015a). This would lower the temperature observed even if the bulk of the scattering occurs away from our line of sight, such that $T_{\rm col} = f_{\rm ds} T_{\rm obs}$, where $f_{\rm ds} \geq 1$ (we parametrize this separately as $f_{\rm ds}$ to make the distinction with $f_{\rm col}$). As the wind launching radius should increase with increasing accretion rate (see Section 4.5), we might expect a scenario in which there the down-scattering introduces a larger effect at higher luminosities, such

[4]This is conceptually similar to the possibility of the cooler outer disc blocking the hotter inner regions discussed in Section 4.2, but here some emission from the inner regions is still able to be transmitted to the observer.
[5]Formally Pinto et al. (2016) also find that a highly ionized absorber with a very large column density ($N_{\rm H} \sim 10^{24}$ cm^{-2}) provides a significant improvement to the fit for the archival *XMM–Newton* data when allowed to have a large blueshift as well as very large velocity broadening. However, the continuum model used in that work did not properly incorporate the high-energy curvature known to be present in ULX spectra (e.g. Gladstone et al. 2009; Walton et al. 2018c), and robustly confirmed by *NuSTAR* for NGC 1313 X-1 (Bachetti et al. 2013); instead of modelling discrete atomic features, this ionized absorption component primarily served to introduce the required high-energy curvature into the continuum at the highest energies probed by *XMM–Newton*. Indeed, re-analysis of these data with a more suitable continuum model finds no evidence for an absorption component with these properties (Pinto et al. 2020).

that $f_{\rm ds} \propto L^{\gamma}$ with $\gamma > 0$. For a given luminosity–temperature relationship prior to any down-scattering of the form $L \propto T_{\rm col}^{\alpha}$, and neglecting the effects of beaming here, we find that increasingly strong down-scattering at higher luminosities should modify the observed luminosity–temperature relation to $L \propto T_{\rm obs}^{\alpha/(1-\alpha\gamma)}$. This kind of down-scattering relation would therefore either steepen the observed luminosity–temperature relation if the trend remains positive (since this requires $\alpha\gamma < 1$), or reverse the trend to give a *negative* luminosity–temperature relation. This may therefore provide another means by which it would be possible to have observed $L_{\rm obs} \propto T_{\rm obs}^{4}$ even if $L_{\rm int} \propto T_{\rm int}^{2}$. However, as with all of the other scenarios considered, producing the two groups of observations would require a sharp jump in the degree to which down-scattering influences the observed emission, and our naive expectation is that this should vary smoothly with accretion rate. Furthermore, reprocessing of the emission from the inner regions by the outer disc/wind is generally considered to be related to the lowest temperature emission (i.e. the DISKBB component) given the apparent connection between ULXs and ultraluminous supersoft sources (ULSs; e.g. Urquhart & Soria 2016; Pinto et al. 2017).

4.5 Super-Eddington X-ray binaries: key radii

Having considered a variety of different possible mechanisms by which the two luminosity–temperature tracks could be produced by either geometric or atmospheric corrections to the inner disc emission, none of which are particularly compelling, we now consider the possibility that we are seeing further distinct key radii/regions of the accretion flow even within the energy range covered by the DISKPBB component in our models. For super-Eddington accretion on to either a black hole or a neutron star there are several key radii to consider: the inner edge of the disc, the spherization radius ($R_{\rm sp}$; the point at which the disc transitions from a standard thin outer disc to the thick inner disc expected for super-Eddington accretion, which should also correspond to the point at which strong, radiatively driven winds start to be launched), and the photon trapping radius ($R_{\rm trap}$, the radius interior to which photons are primarily advected inwards rather than released locally; note that $R_{\rm trap} < R_{\rm sp}$, Poutanen et al. 2007).

4.5.1 *Black hole accretor*

For a black hole accretor, the accretion disc is expected to extend in to the innermost stable circular orbit ($R_{\rm ISCO}$) at high accretion rates. This is set purely by the mass and spin of the black hole, neither of which can be changing significantly over the course of the observations considered here, so the inner regions of the accretion flow would be expected to have a constant inner radius even if the accretion rate on to the black hole changes. $R_{\rm ISCO}$ would therefore be a natural candidate for the smaller of the two potential stable radii in NGC 1313 X-1 ($R_{\rm in,2}$; we note again that, even if $L \propto T^2$ for these observations, this would imply a stable inner radius if the disc is in the advection-dominated regime). Indeed, the rough estimates for the absolute value of this radius are appropriate for the innermost stable circular orbit of a typical $10\,{\rm M}_{\odot}$ black hole, depending on its spin.

However, in contrast to $R_{\rm ISCO}$, based on standard accretion theory the spherization radius is expected to scale with the accretion rate, i.e. $R_{\rm sp} \propto \dot{m}$ (where $\dot{m}$ is the accretion rate in units of the Eddington accretion rate; Shakura & Sunyaev 1973; Poutanen et al. 2007). The trapping radius is also expected to have a similar dependence, i.e. $R_{\rm trap} \propto \dot{m}$ (Lasota 2016). Should the lower temperature track exhibit a constant radius, and be related to either of these radii in the flow, this would imply that the accretion rate is constant. However, changes in $\dot{m}$ are almost certainly required to produce the flux and temperature variations observed. Allowing instead for a varying emitting radius that increases with luminosity, as would be expected for both $R_{\rm sp}$ and $R_{\rm trap}$, we can write $R \propto L^{\delta}$ (where $\delta > 0$), and show that in this case $L \propto T^{4/(1-2\delta)}$ (assuming $L \propto R^2T^4$, since we are considering the regions outside $R_{\rm trap}$). This scenario should either again steepen the observed luminosity–temperature relation away from $L \propto T^4$ (for $0 < \delta < 0.5$) or even reverse the trend such that $L_{\rm obs}$ and T are anticorrelated (for $\delta > 0.5$). Given that positive correlations are observed, we may therefore expect the lower temperature track to have a steeper luminosity–temperature relation than the higher temperature track if this is associated with either $R_{\rm sp}$ or $R_{\rm trap}$, particularly if the inner regions vary as $L \propto T^2$. Although the data do not obviously require this, given the limited observations we cannot exclude this possibility (and there is maybe a weak hint that this is the case for the results from the magnetic model). However, if the effects of e.g. beaming are more pronounced for the higher temperature track, then this difference could be reduced.

Assuming that the DISKBB component comes from the disc/wind at the transition to the super-Eddington flow at $R_{\rm sp}$, one interesting possibility is therefore that we are seeing a further transition in the disc at $R_{\rm trap}$ manifested in the behaviour of the DISKPBB component. The decreased variability at high energies could then be a result of higher accretion rates leading to both stronger winds and increased photon trapping, such that mass accretion rate fluctuations in the outer disc lead to a much weaker response than would naively be expected from the inner regions, as discussed in Middleton et al. (2015a). This could also be qualitatively similar to the high-energy 'saturation' effects discussed by Feng et al. (2019).

4.5.2 *Non-magnetic neutron star accretor*

For a neutron star accretor, the inner edge of the accretion flow is set by either the surface of the neutron star for non- or weakly magnetized neutron stars (modulo the presence of any boundary layer; the innermost stable circular orbit is likely similar to or smaller than the radius expected for a typical neutron star: $R_{\rm ISCO} \sim 12\,{\rm km}$, while $R_{\rm NS} \sim 13\,{\rm km}$; Miller et al. 2019; Riley et al. 2019) or the magnetospheric radius for strongly magnetized neutron stars ($R_{\rm M}$; the point at which the magnetic field of the neutron star truncates the disc and the in-falling material is forced to follow the field lines instead). Similar to $R_{\rm ISCO}$, the radius of the neutron star cannot be evolving significantly over the course of our observations, so this may also be a plausible explanation for one of the potentially stable radii if the neutron star is non-magnetic. While the value of the inner radius estimated for the smaller of the two potential stable radii ($R_{\rm in,2}$) is larger than the characteristic radius expected for a neutron star, it may still be possible for the potential geometric beaming effects discussed above to bring the two into consistency (although this would require $0.05 \lesssim b \lesssim 1$, depending on $f_{\rm col}$ and i, and the lower end of this range would represent moderately extreme beaming).

However, unlike the black hole case, radiation cannot be advected over the horizon here; while advection may still be a relevant process within some regions of the disc, this radiation must emerge somewhere, presumably in the boundary layer where the disc meets the neutron star surface. If this boundary layer behaves as an

extension of the disc, it is not clear that it would be possible for such a scenario to produce an $L \propto T^2$ scaling; even with advection $L \propto T^4$ may be expected in this case. Alternatively, though, this boundary layer may be the origin of the highest energy emission observed by *NuSTAR* (i.e. $E > 10$ keV), as the material shocks at the neutron star surface. If this is the case, it may still be possible for an advection-dominated disc around a neutron star to produce $L \propto T^2$, and we may again expect the lower temperature track to have a steeper luminosity–temperature relation. However, in this case the lack of long-term high-energy variability would likely imply that the winds are removing the majority of any accretion rate fluctuations before they reach these regions (Middleton et al. 2015a).

4.5.3 Magnetic neutron star accretor

In the classic picture of accretion on to a magnetized neutron star, $R_{\rm in} = R_{\rm M}$, and $R_{\rm M}$ is set by the combination of the magnetic field of the neutron star and the accretion rate: $R_{\rm M} \propto B^{4/7}\dot{M}^{-2/7}$ (Lamb, Pethick & Pines 1973; Cui 1997). However, this assumes that the disc is gas-pressure dominated, which is not expected to be the case for super-Eddington accretion. Chashkina et al. (2019) construct a model for accretion on to a magnetized neutron star that extends to high accretion rates, building on their previous model that accounts for radiation pressure (Chashkina, Abolmasov & Poutanen 2017) by further incorporating the effects of advection and outflows following the prescription of Poutanen et al. (2007). Within this framework, at low accretion rates the disc is dominated by gas pressure, then as the accretion rate increases the disc becomes dominated by radiation pressure, and as the accretion rate increases further, the disc eventually becomes dominated by the effects of advection. At low accretion rates, Chashkina et al. (2019) find that the evolution of $R_{\rm M}$ with accretion rate does follow something close to the model of Lamb et al. (1973). Interestingly, though, while the disc is in the radiation-pressure dominated regime Chashkina et al. (2019) find that $R_{\rm M}$ actually becomes constant with varying accretion rate, before exhibiting a weak dependence again when the disc becomes advection dominated (although in this latter case the dependence is weaker than that seen in the gas-pressure regime). During the radiation-pressure-dominated regime, instead of pushing $R_{\rm M}$ further in, the increase in accretion rate instead primarily causes the scale height of the disc outside of $R_{\rm M}$ to increase, and the dependence of $R_{\rm M}$ on accretion rate re-appears in the advection-dominated regime because the local Eddington limit then prevents the scale height of the disc increasing beyond $H/R \sim 1$ (see also Lasota et al. 2016).

Emission from a radiation-pressure dominated accretion disc around a magnetized neutron star may therefore offer another promising explanation if the innermost radius of the disc is stable. In this scenario, we would have $R_{\rm M} > R_{\rm trap}$, and so we would expect the disc to vary intrinsically as $L \propto T^4$. By itself, this would not explain the two luminosity–temperature tracks, but Mushtukov et al. (2015) suggest that the accretion curtains that link the disc outside $R_{\rm M}$ to the central accretion columns may be optically thick for the super-Eddington accretion seen in the known ULX pulsars, and would thus emit multicolour blackbody spectra, which could also potentially provide the hotter DISKPBB track in this scenario. However, in this case the scale-height of the inner disc would be variable, resulting in variable collimation for the emission arising from regions interior to $R_{\rm M}$. In this case, we may therefore expect the hotter luminosity–temperature track to exhibit a steeper scaling, but if anything the opposite currently appears more likely.

Alternatively, if the disc were advection-dominated in this scenario ($R_{\rm trap} > R_{\rm M}$), we would now be in a situation where the inner radius would decrease with increasing luminosity (as opposed to the non-magnetic cases where it remained constant). This would correspond to $\delta < 0$, following our earlier notation. Therefore, it may be that a luminosity–temperature relation even flatter than $L \propto T^2$ would be expected in this case. Assuming the lower temperature track relates to regions outside of $R_{\rm trap}$, the expectation that these data would show a steeper luminosity–temperature relationship would therefore be even stronger. Again, we note that there is a weak indication this may be the case with the current data and the magnetic accretor model.

Any radiation advected through the disc in this scenario would also escape from the inner walls of the truncated, large scale height flow at $R_{\rm M}$. If the surface and mid-plane temperatures of the disc differ significantly (as may be the case if $f_{\rm col} \sim 3$), and a significant fraction of the intrinsic flux is advected, then this could appear as a distinct component in the observed spectrum at lower temperatures than the innermost emission from the surface. It may even be possible that this emission is the cause for the two luminosity–temperature tracks, particularly if it is strongly enhanced via beaming. However, this would require that the advected emission through the disc be more variable than the emission from the upper surface. In turn, this would suggest that strong accretion rate fluctuations are surviving through to $R_{\rm M}$, such that similarly strong variability may again be expected for the accretion column, contrary to what is observed. Nevertheless, even if this emission does not dominate the lower temperature observations, it may make a non-negligible contribution. Assuming instead that the lower temperature track primarily represents emission from larger radii, as long as changes in the wind can efficiently prevent changes in the accretion rate from reaching the innermost regions (Middleton et al. 2015a), it may still be possible to explain the reduced high-energy variability.

Given the arguments presented above, should both tracks imply stable radii, it is also tempting to consider a scenario in which the inner radius of a radiation-pressure-dominated disc transitions between the magnetosphere and the surface of the neutron star. Indeed, recent simulations of accretion on to magnetized neutron stars show two distinct regimes for actively accreting neutron stars (Parfrey & Tchekhovskoy 2017; Parfrey, Spitkovsky & Beloborodov 2017). One is the 'standard' regime in which the magnetic field truncates the accretion flow at $R_{\rm M}$, forcing the in-falling material along the field lines, while at even higher accretion rates the accreting material fully crushes the magnetosphere, and the disc extends in to the surface of the neutron star. If a neutron star accretor can sharply transition between these two regimes it may be possible to produce two well-defined groups of observations that each follow separate luminosity–temperature tracks. However, in any scenario along these lines we would expect to see the smaller of the two stable inner radii to be associated with the higher luminosity observations, which as noted previously is not the case. Furthermore, the two states simulated by Parfrey & Tchekhovskoy (2017) likely represent two snapshots of the gradual evolution of the magnetospheric radius with accretion rate described by Chashkina et al. (2019),[6] so it is

[6]It is worth noting that the simulations presented by Parfrey & Tchekhovskoy (2017) do not include radiation, and so cannot formally reproduce the radiation-pressure-dominated regime described by Chashkina et al. (2019). Initial efforts to include radiation in such have been undertaken by Takahashi & Ohsuga (2017), but currently only a single accretion rate has been presented.

not clear that a sharp transition between these states should be expected in any case. Lastly, the lack of strong variability is likely also problematic for this scenario, as the central accretion columns producing the high-energy emission would not likely be present if the magnetosphere were fully crushed.

5 SUMMARY AND CONCLUSIONS

We have presented results from the major coordinated X-ray observing programme on the ULX NGC 1313 X-1 performed in 2017, combining *XMM–Newton*, *Chandra*, and *NuSTAR*, focusing on the evolution of the broad-band (∼0.3–30.0 keV) continuum emission. Clear spectral variability is observed, but this is markedly suppressed above ∼10–15 keV. This is qualitatively similar to the broad-band spectral evolution seen in Holmberg IX X-1. Furthermore, when fit with accretion disc models designed to represent super-Eddington accretion, the various observations trace out two distinct tracks in the luminosity–temperature plane. Larger emitting radii and lower temperatures are seen at higher observed fluxes. However, each of these tracks individually show positive correlations between L and T, and are consistent with an $L \propto T^4$ scaling, as would be expected for blackbody emission with a constant emitting area, and also with an $L \propto T^2$ scaling, as may be expected for an advection-dominated disc around a black hole accretor. The limited dynamic range covered for each track currently prevents us from distinguishing between these possibilities; further broad-band observations spanning a broader range in flux are required to confirm the precise nature of these luminosity–temperature relations.

We have considered a variety of different possible scenarios that may be relevant for super-Eddington accretion on to NGC 1313 X-1 in order to try and explain this unusual behaviour, allowing for both a neutron star and a black hole accretor (since the nature of the system is not known at the current time). These include geometric changes (precession of the flow, beaming of the radiation, obscuration of the inner regions), as well as atmospheric effects (colour correction in the disc atmosphere, down-scattering in the wind). However, based on our current understanding, the majority of these are expected to vary smoothly with accretion rate, making it challenging to produce the sharp transition required to explain the two luminosity–temperature tracks, and many would predict that higher temperatures should be seen at higher luminosities, in contrast to the observations. One of the more promising scenarios among this set with regards to the luminosity–temperature behaviour is that, as the accretion rate increases, the scale height of the outer disc/wind also increases (as expected for super-Eddington accretion) and blocks some of the inner (and hottest) regions from view. However, this is difficult to reconcile with the reduced level of variability at the highest energies, under the typical assumption that this emission arises from the most compact regions (either in a central Compton scattering corona or an accretion column). Should this be the cause of the luminosity–temperature behaviour, we may need to invoke other origins for the highest energy emission, e.g. bulk-motion Comptonization in the more extended, diverging outflow.

Alternatively, it may be that we are seeing evidence for even further radial stratification of the flow than included in our simple two-component model for the thermal emission from the disc/wind. One interesting possibility here is that we are seeing evidence for a further transition in the disc at the photon trapping radius, in addition to the spherization radius. This could plausibly explain both the two distinct luminosity–temperature tracks, and through a combination of outflows and advection, explain the suppressed variability seen at the highest energies.

ACKNOWLEDGEMENTS

The authors would like to thank the reviewer for their positive and thorough feedback, which helped to improve the final version of this manuscript. DJW and MJM acknowledge support from Science and Technology Facilities Council (STFC) Ernest Rutherford Fellowships. CP and FF acknowledge support from European Space Agency (ESA) Research Fellowships. HPE acknowledges support under National Aeronautics and Space Administration (NASA) contract NNG08FD60C. TPR was funded as part of the STFC consolidated grant ST/K000861/1. NW acknowledges support from Centre National d'Etudes Spatiales (CNES) for this work. CRC and MN acknowledge support from the Smithsonian Astrophysical Observatory (SAO) contract SV3-73016 to the Massachusetts Institute of Technology (MIT), which is in turn supported by NASA under contract NAS8-03060 for the *Chandra* X-ray Center (CXC). This research has made use of data obtained with *NuSTAR*, a project led by Caltech, funded by NASA and managed by NASA Jet Propulsion Laboratory (JPL), and has utilized the NUSTARDAS software package, jointly developed by the Space Science Data Centre (SSDC; Italy) and Caltech (USA). This research has also made use of data obtained with *XMM–Newton*, an ESA science mission with instruments and contributions directly funded by ESA Member States.

REFERENCES

Abe Y., Fukazawa Y., Kubota A., Kasama D., Makishima K., 2005, PASJ, 57, 629
Abramowicz M. A., Czerny B., Lasota J. P., Szuszkiewicz E., 1988, ApJ, 332, 646
Andersen B. C., Ransom S. M., 2018, ApJ, 863, L13
Annuar A. et al., 2015, ApJ, 815, 36
Arnaud K. A., 1996, in Jacoby G. H., Barnes J., eds, ASP Conf. Ser. Vol. 101, Astronomical Data Analysis Software and Systems V. Astron. Soc. Pac., San Francisco, p. 17
Bachetti M. et al., 2013, ApJ, 778, 163
Bachetti M. et al., 2014, Nature, 514, 202
Brightman M. et al., 2016, ApJ, 816, 60
Brightman M . et al., 2018, Nat. Astron., 2, 312
Canizares C. R. et al., 2005, PASP, 117, 1144
Carpano S., Haberl F., Maitra C., Vasilopoulos G., 2018, MNRAS, 476, L45
Chashkina A., Abolmasov P., Poutanen J., 2017, MNRAS, 470, 2799
Chashkina A., Lipunova G., Abolmasov P., Poutanen J., 2019, A&A, 626, A18
Cui W., 1997, ApJ, 482, L163
Dall'Osso S., Perna R., Stella L., 2015, MNRAS, 449, 2144
Davis J. E., 2001, ApJ, 562, 575
Davis S. W., El-Abd S., 2019, ApJ, 874, 23
den Herder J. W. et al., 2001, A&A, 365, L7
Dotan C., Shaviv N. J., 2011, MNRAS, 413, 1623
Earnshaw H. P., Roberts T. P., Sathyaprakash R., 2018, MNRAS, 476, 4272
Evans P. A. et al., 2009, MNRAS, 397, 1177
Feng J., Cao X., Gu W.-M., Ma R.-Y., 2019, ApJ, 885, 93
Fürst F. et al., 2016, ApJ, 831, L14
Fürst F., Walton D. J., Stern D., Bachetti M., Barret D., Brightman M., Harrison F. A., Rana V., 2017, ApJ, 834, 77
Fürst F. et al., 2018, A&A, 620, A153
Gehrels N. et al., 2004, ApJ, 611, 1005
Gladstone J. C., Roberts T. P., Done C., 2009, MNRAS, 397, 1836
Haardt F., Maraschi L., 1991, ApJ, 380, L51
Harrison F. A., Craig W. W., Christensen F. E. et al., 2013, ApJ, 770, 103

Houck J. C., Denicola L. A., 2000, in ASP Conf. Ser. Vol. 216: Astronomical Data Analysis Software and Systems IX. Astron. Soc. Pac., San Francisco, p. 591
Huenemoerder D. P. et al., 2011, AJ, 141, 129
Huppenkothen D. et al., 2019, ApJ, 881, 39
Israel G. L., Belfiore A., Stella L. et al., 2017a, Science, 355, 817
Israel G. L., Papitto A., Esposito P. et al., 2017b, MNRAS, 466, L48
Jansen F. et al., 2001, A&A, 365, L1
Kaaret P., Feng H., Roberts T. P., 2017, ARA&A, 55, 303
Kalberla P. M. W., Burton W. B., Hartmann D., Arnal E. M., Bajaja E., Morras R., Pöppel W. G. L., 2005, A&A, 440, 775
Kara E. et al., 2020, MNRAS, 491, 5172
King A. R., 2008, MNRAS, 385, L113
King A. R., 2009, MNRAS, 393, L41
King A. R., Pounds K. A., 2003, MNRAS, 345, 657
Kluźniak W., Lasota J.-P., 2015, MNRAS, 448, L43
Koliopanos F., Vasilopoulos G., Godet O., Bachetti M., Webb N. A., Barret D., 2017, A&A, 608, A47
Kosec P., Pinto C., Fabian A. C., Walton D. J., 2018a, MNRAS, 473, 5680
Kosec P., Pinto C., Walton D. J., Fabian A. C., Bachetti M., Brightman M., Fürst F., Grefenstette B. W. et al., 2018b, MNRAS, 479, 3978
Krivonos R., Sazonov S., 2016, MNRAS, 463, 756
Kubota A., Makishima K., 2004, ApJ, 601, 428
Kubota A., Tanaka Y., Makishima K., Ueda Y., Dotani T., Inoue H., Yamaoka K. et al., 1998, PASJ, 50, 667
Lamb F. K., Pethick C. J., Pines D., 1973, ApJ, 184, 271
Lasota J.-P., 2016, in Bambi C., ed., Astrophysics and Space Science Library, Vol. 440, Astrophysics of Black Holes: From Fundamental Aspects to Latest Developments, Springer, Verlag, Berlin, p. 1
Lasota J.-P., Vieira R. S. S., Sadowski A., Narayan R., Abramowicz M. A., 2016, A&A, 587, A13
Luangtip W., Roberts T. P., Done C., 2016, MNRAS, 460, 4417
Madsen K. K. et al., 2015, ApJS, 220, 8
Méndez B., Davis M., Moustakas J., Newman J., Madore B. F., Freedman W. L., 2002, AJ, 124, 213
Middleton M. J., Walton D. J., Roberts T. P., Heil L., 2014, MNRAS, 438, L51
Middleton M. J., Heil L., Pintore F., Walton D. J., Roberts T. P., 2015a, MNRAS, 447, 3243
Middleton M. J . et al., 2015b, MNRAS, 454, 3134
Middleton M. J. et al., 2018, MNRAS, 475, 154
Middleton M. J., Brightman M., Pintore F., Bachetti M., Fabian A. C., Fürst F., Walton D. J., 2019, MNRAS, 486, 2
Miller M. C., Colbert E. J. M., 2004, Int. J. Mod. Phys. D, 13, 1
Miller J. M., Fabbiano G., Miller M. C., Fabian A. C., 2003, ApJ, 585, L37
Miller J. M., Fabian A. C., Miller M. C., 2004, ApJ, 607, 931
Miller J. M., Walton D. J., King A. L., Reynolds M. T., Fabian A. C., Miller M. C., Reis R. C., 2013, ApJ, 776, L36
Miller J. M., Bachetti M., Barret D., Harrison F. A., Fabian A. C., Webb N. A., Walton D. J., Rana V., 2014, ApJ, 785, L7
Miller M. C . et al., 2019, ApJ, 887, L24
Mineshige S., Hirano A., Kitamoto S., Yamada T. T., Fukue J., 1994, ApJ, 426, 308
Mitsuda K. et al., 1984, PASJ, 36, 741
Mukherjee E. S. et al., 2015, ApJ, 808, 64
Mushtukov A. A., Suleimanov V. F., Tsygankov S. S., Poutanen J., 2015, MNRAS, 454, 2539
Mushtukov A. A., Ingram A., Middleton M., Nagirner D. I., van der Klis M., 2019, MNRAS, 484, 687
Ohsuga K., Mineshige S., 2011, ApJ, 736, 2
Parfrey K., Tchekhovskoy A., 2017, ApJ, 851, L34
Parfrey K., Spitkovsky A., Beloborodov A. M., 2017, MNRAS, 469, 3656
Pinto C., Middleton M. J., Fabian A. C., 2016, Nature, 533, 64
Pinto C. et al., 2017, MNRAS, 468, 2865
Pinto C. et al., 2020, MNRAS, 492, 4646
Pintore F., Zampieri L., Stella L., Wolter A., Mereghetti S., Israel G. L., 2017, ApJ, 836, 113
Poutanen J., Lipunova G., Fabrika S., Butkevich A. G., Abolmasov P., 2007, MNRAS, 377, 1187
Rana V. et al., 2015, ApJ, 799, 121
Ransom S. M., Eikenberry S. S., Middleditch J., 2002, AJ, 124, 1788
Reis R. C., Miller J. M., 2013, ApJ, 769, L7
Riley T. E . et al., 2019, ApJ, 887, L21
Rodríguez Castillo G. A., Israel G. L., Belfiore A. et al., 2019, ApJ, in press, preprint (arXiv:1906.04791)
Sathyaprakash R. et al., 2019, MNRAS, 488, L35
Sazonov S. Y., Lutovinov A. A., Krivonos R. A., 2014, Astron. Lett., 40, 65
Shakura N. I., Sunyaev R. A., 1973, A&A, 24, 337
Shidatsu M., Ueda Y., Fabrika S., 2017, ApJ, 839, 46
Shimura T., Takahara F., 1995, ApJ, 445, 780
Song X., Walton D. J., Lansbury G. B., Evans P. A., Fabian A. C., Earnshaw H., Roberts T. P., 2020, MNRAS, 491, 1260
Soria R., Wu K., Kunic Z., 2008, in Carpano S., Ehle M., Pietsch W., eds, X-rays From Nearby Galaxies, MPE Report series, Garching, p. 48
Steiner J. F., Narayan R., McClintock J. E., Ebisawa K., 2009, PASP, 121, 1279
Stobbart A.-M., Roberts T. P., Wilms J., 2006, MNRAS, 368, 397
Strohmayer T. E., Mushotzky R. F., 2009, ApJ, 703, 1386
Strüder L. et al., 2001, A&A, 365, L18
Takahashi H. R., Ohsuga K., 2017, ApJ, 845, L9
Takeuchi S., Ohsuga K., Mineshige S., 2013, PASJ, 65, 88
Tully R. B., Courtois H. M., Sorce J. G., 2016, AJ, 152, 50
Turner M. J. L. et al., 2001, A&A, 365, L27
Urquhart R., Soria R., 2016, MNRAS, 456, 1859
Vasilopoulos G., Haberl F., Carpano S., Maitra C., 2018, A&A, 620, L12
Verner D. A., Ferland G. J., Korista K. T., Yakovlev D. G., 1996, ApJ, 465, 487
Vierdayanti K., Watarai K.-Y., Mineshige S., 2008, PASJ, 60, 653
Walton D. J. et al., 2013, ApJ, 779, 148
Walton D. J. et al., 2014, ApJ, 793, 21
Walton D. J . et al., 2015a, ApJ, 799, 122
Walton D. J . et al., 2015b, ApJ, 806, 65
Walton D. J . et al., 2016a, ApJ, 826, L26
Walton D. J. et al., 2016b, ApJ, 826, 87
Walton D. J. et al., 2017, ApJ, 839, 105
Walton D. J. et al., 2018a, ApJ, 857, L3
Walton D. J. et al., 2018b, MNRAS, 473, 4360
Walton D. J., Fürst F., Heida M. et al., 2018c, ApJ, 856, 128
Watarai K.-y., Mineshige S., 2003, ApJ, 596, 421
Watarai K.-y., Fukue J., Takeuchi M., Mineshige S., 2000, PASJ, 52, 133
Weisskopf M. C., Brinkman B., Canizares C., Garmire G., Murray S., Van Speybroeck L. P., 2002, PASP, 114, 1
Wilms J., Allen A., McCray R., 2000, ApJ, 542, 914
Zhou Y., Feng H., Ho L. C., Yao Y., 2019, ApJ, 871, 115

APPENDIX A: PULSATION SEARCHES

We have undertaken basic pulsation searches for all of the 2017 observations of NGC 1313 X-1 taken with high time resolution instruments (i.e. *XMM–Newton* and *NuSTAR*). To do so, all times were transferred to the solar barycentre using the DE200 solar ephemeris. For the *XMM–Newton* observations, we then scanned all the available EPIC-pn light curves (including both the 2017 campaign and archival data sets) for pulsations by following the procedure implemented in Sathyaprakash et al. (2019). We did not find any significant detections above the 3σ confidence level, and all the candidate signals below this threshold were found to have substantially different frequencies (above $\sim$1 Hz).

We also ran a timing analysis to search for pulsations in the data from all *NuSTAR* OBSIDs. First, we estimated the power density spectrum in all these observations. Each of the observations were divided into 512-s segments, each of which was defined to be fully covered by the *NuSTAR* good time intervals in order to avoid spuri-

ous frequencies arising from the aliasing of orbital occultation gaps. We then averaged the PDS calculated in each segment and looked for signals exceeding the false-alarm probability of white noise, taking into account the number of trials (i.e. the number of spectral points). This was done using HENDRICS (based on STINGRAY; Huppenkothen et al. 2019), but did not return any significant signals. We also ran an accelerated search for pulsations using the PRESTO software package (Ransom, Eikenberry & Middleditch 2002). After creating light curves with a binning time of 0.1 ms, we produced binary files compatible with PRESTO. We ran the ACCELSEARCH tool, with and without the search over a second derivative (a Jerk search; Andersen & Ransom 2018). All candidates from the accelerated search were analysed with the PREPFOLD tool and the diagnostic plots were inspected by eye. The majority of the low-significance candidate pulsations are beats of the sampling frequency and an instrumental 890 Hz oscillation (related to *NuSTAR* housekeeping operations). They are distributed on a continuum, power-law-like spectrum in the sigma versus spin period plot, so that they form a 'noise' level to which we can compare credible candidates. The higher significance candidates (exceeding the previously described noise level) have very low periods, none of which are consistent between observations or even between different segments of the same data set. These are all found to be aliases of the orbital occultation data gaps (there is currently no way in PRESTO to correct for these missing data).

[1]*Institute of Astronomy, University of Cambridge, Madingley Road, Cambridge CB3 0HA, UK*
[2]*ESTEC/ESA, Keplerlaan 1, NL-2201AZ Noordwijk, the Netherlands*
[3]*INAF – IASF Palermo, Via U. La Malfa 153, I-90146 Palermo, Italy*
[4]*Physics Department, CB 1105, Washington University, One Brookings Drive, St. Louis, MO 63130-4899, USA*
[5]*INAF-Osservatorio Astronomico di Cagliari, via della Scienza 5, I-09047 Selargius, Italy*
[6]*Centre for Extragalactic Astronomy, Department of Physics, Durham University, South Road, Durham DH1 3LE, UK*
[7]*MIT Kavli Institute for Astrophysics and Space Research, Cambridge, MA 02139, USA*
[8]*College of Astronomy and Space Sciences, University of the Chinese Academy of Sciences, Beijing 100049, China*
[9]*Sydney Institute for Astronomy, School of Physics A28, The University of Sydney, Sydney, NSW 2006, Australia*
[10]*Space Radiation Laboratory, California Institute of Technology, Pasadena, CA 91125, USA*
[11]*European Space Astronomy Centre (ESA/ESAC), Operations Department, E-28691 Villanueva de la Cañada, Madrid, Spain*
[12]*European Southern Observatory, Karl-Schwarzschild-Straβe 2, D-85748 Garching bei München, Germany*
[13]*Department of Physics and Astronomy, University of Southampton, Highfield, Southampton SO17 1BJ, UK*
[14]*Jet Propulsion Laboratory, California Institute of Technology, Pasadena, CA 91109, USA*
[15]*Key Laboratory of Particle Astrophysics, Institute of High Energy Physics, Chinese Academy of Sciences, Beijing 100049, China*
[16]*IRAP, Université de Toulouse, CNRS, CNES, 9 avenue du Colonel Roche, F-31028 Toulouse, France*

This paper has been typeset from a TEX/LATEX file prepared by the author.